https://dx.doi.org/10.1016/j.jobe.2022.105212

Mechanical analysis and finite element modeling of FRP-ECC-HSC composite stub column under axial compression

Shuai Li Tak-Ming Chan* Ben Young

Department of Civil and Environmental Engineering, The Hong Kong Polytechnic University, Hong Kong, China

*Corresponding author.

Email address: tak-ming.chan@polyu.edu.hk (T.-M. Chan).

Abstract

A novel composite column, consisting of an outer fiber-reinforced polymer (FRP) tube, an inner high strength concrete (HSC) core and an engineered cementitious composite (ECC) ring, has been proposed and investigated. Compared with normal FRP-confined HSC column, the FRP-ECC-HSC composite column could exhibit superior deformability performance. In this study, mechanical analysis was firstly conducted on the composite column to investigate the interaction behavior among different components, i.e. HSC core, ECC ring and FRP tube. Modified analysis-oriented models were proposed for HSC and ECC under uniform FRP confinement. Furthermore, finite element (FE) models were also established with the use of accurate concrete damaged plasticity (CDP) model to simulate the behavior of the composite column, especially the ECC ring which is under non-uniform confinement. The material property data used in the FE models were generated by the modified analysis-oriented models. It is shown that the FE models can provide close predictions on the axial load-axial strain behavior and hoop strain-axial strain behavior compared with test results. Meanwhile, stress distribution over the composite column section as well as the influence of ECC ratio were discussed with the validated FE model.

Keywords: FRP-ECC-HSC, composite column, non-uniform confinement, mechanical analysis, finite element model

1. Introduction

In recent years, fiber-reinforced polymer (FRP) confined high strength concrete (HSC) column is widely investigated in research and has been applied in engineering practice. The structural behavior, including both compressive loading capacity and deformability, can be effectively improved compared with unconfined HSC columns [1-3]. However, due to the highly brittle nature of HSC under compression, localized FRP rupture may occur, leading to premature failure of the column [4]. A novel composite column, consisting of an outer FRP tube, an inner HSC core and an engineered cementitious composite (ECC) ring, has been proposed and experimentally investigated under axial compression by the authors [5]. It shows that the ECC ring could effectively redistribute the strain from HSC core to FRP tube, leading to a more uniform hoop strain on the FRP tube. Column failure is delayed with an improved ultimate axial compressive strain. Consequently, the FRP-ECC-HSC composite column could develop better deformability in comparison to the normal FRP-confined HSC column.

Extensive analysis-oriented models have been proposed to predict the axial compressive behavior of FRP-confined concrete [6-10]. Researchers consider the interaction behavior of confining FRP and confined concrete, with equations describing the relations among axial stress, axial strain, hoop strain and confining pressure. Jiang and Teng's model [6] was developed based on a large database of FRP-confined normal strength concrete and has been widely accepted, while Lim and Ozbakkaloglu [7] conducted a series of tests on FRP-confined HSC and proposed the corresponding analysis model, which is more suitable for high strength concrete. However, these models are only applicable to uniformly FRP-confined concrete, which is with circular cross-section. For FRP-confined concrete with rectangular, square, elliptical or annular sections, the concrete is under non-uniform confinement and the compressive stress-strain behavior cannot be given directly by the analysis-oriented models [11,12]. Design-oriented model, which is directly regressed based on test results, is another

approach for FRP-confined concrete [13,14]. However, design models are highly empirical and cannot provide accurate predictions if the test database is limited. Finite element (FE) modeling is an approach which could be adopted when analysis-oriented models and design-oriented models cannot be directly used for FRP-confined concrete, especially for the cases of non-uniform confinement [11,15-21]. Yu et al. [15,16] established confined concrete properties with concrete damaged plasticity (CDP) model in ABAUQS to simulate the axial compressive behavior of FRP-confined concrete of square and annular sections. It was found that good agreements on axial stress-axial strain relations and hoop strain-axial strain relations could be obtained compared with test results. Lo et al. [17] conducted finite element analysis on FRP-confined rectangular concrete columns under axial compression and numerically assessed the non-uniform effects in the rectangular sections. Ribeiro et al. [18] and Zeng et al. [19] established the three-dimensional finite element model to simulate the compressive behavior of FRP-confined concrete. Hany et al. [20] and Li et al. [21] developed the improved concrete damaged plasticity models to generate the material properties of confined concrete with complex stress fields.

FRP-confined ECC, as a composite structural form with advanced concrete material confined with FRP, has not been widely investigated in the current stage. It is noted that the dilation behavior of FRP-confined ECC is different from that of FRP-confined normal concrete under axial compression, due to the presence of fiber in ECC mix. Li et al. [22] experimentally investigated the compressive behavior of ECC under different confining pressures and proposed equations to predict the enhanced compressive strength and strain. Dang et al. [23] compared the structural performance between FRP-confined ECC cylinders and FRP-confined normal concrete cylinders and developed prediction models for the ultimate conditions. Yuan et al. [24] evaluated the existing hoop strain-axial strain models for FRP-confined ECC against test results and proposed the modified models. Li et al. [25] recently developed a novel FRP-

concrete double tube composite column and compared the compressive behavior of the columns with normal concrete or ECC as the ring concrete. It was reported that the columns with ECC ring had the slower development of lateral dilation and could achieve an improved ultimate column deformability. Based on the current research, the analysis and design models for FRP-confined normal concrete may not be applicable to FRP-confined ECC [23,24]. Therefore, it is worth carrying out more studies on FRP-confined ECC to develop suitable prediction models.

Experimental investigations on the FRP-ECC-HSC composite column under axial compression have been conducted by the authors [5]. Detailed information of the tested specimens is listed in Table 1. For FRP-ECC-HSC composite column, the mechanism is more complicated due to two types of concrete involved. HSC core is uniformly confined, while ECC ring is subjected to non-uniform confinement. In this study, mechanical analysis on the composite column was firstly conducted to understand the interaction behavior among FRP tube, ECC ring and HSC core. Analysis-oriented models were developed for FRP-confined HSC and ECC, respectively. FE models were also established with accurate material properties based on the developed analysis-oriented models, and then validated against test results. It is noted that both mechanical analysis and finite element approach were used to investigate the stress distribution and confining pressure in the FRP-ECC-HSC composite column in this study. Mechanical analysis was carried out assuming that the materials were in elastic range, so that Hooke's law could be followed. One the other hand, accurate elastic-plastic material properties for confined concrete were considered in FE models. Therefore, results obtained through the two approaches cannot be compared directly. However, they can both showcase and help understand the working mechanism of the composite column.

98 Table 1 Details of tested specimens (Adopted from Li et al. [5])

Specimen ID	HSC core				ECC ring				FRP tube	
	Strength (MPa)	Strain	Elastic modulus (MPa)	Diameter (mm)	Strength (MPa)	Strain	Elastic modulus (MPa)	Thickness (mm)	Hoop tensile elastic modulus (MPa)	Thickness (mm)
FH70	75.4	0.0028	32000	200	-	-	-	-	39800	2.5
FH70-R	75.4	0.0028	32000	200	-	-	-	-	39800	2.5
FE50H70-15	75.4	0.0028	32000	170	55.2	0.0046	15300	15	39800	2.5
FE50H70-15-R	75.4	0.0028	32000	170	55.2	0.0046	15300	15	39800	2.5
FE50H70-25	75.4	0.0028	32000	150	55.2	0.0046	15300	25	39800	2.5
FE50H70-25-R	75.4	0.0028	32000	150	55.2	0.0046	15300	25	39800	2.5
FH90	96.8	0.0032	35300	200	-	-	-	-	39800	2.5
FH90-R	96.8	0.0032	35300	200	-	-	-	-	39800	2.5
FE50H90-15	96.8	0.0032	35300	170	55.2	0.0046	15300	15	39800	2.5
FE50H90-15-R	96.8	0.0032	35300	170	55.2	0.0046	15300	15	39800	2.5
FE50H90-25	96.8	0.0032	35300	150	55.2	0.0046	15300	25	39800	2.5
FE50H90-25-R	96.8	0.0032	35300	150	55.2	0.0046	15300	25	39800	2.5

99 Note: “F”, “E” and “H” represent the FRP tube, ECC ring and HSC core, respectively. “50”, “70” and “90” represent the different concrete grades of ECC ring and HSC core.

100 Specimen ID with “R” refers to a repeated specimen.

2. Mechanical analysis

2.1 Stress distribution

For FRP-ECC-HSC composite column under axial compression, as shown in Fig. 1, HSC core and ECC ring are compressed in the axial direction and will expand in the lateral direction. The lateral dilation causes tensile force in FRP tube, which leads to the confining pressure on the inner concrete. Based on the theory of material mechanics [26], stress distribution of the composite column is calculated and presented in this section.

It should be noted that the following calculation is carried out in elastic stage, so that Hooke's law can be used to determine the stress-strain relationship of the material. Plane polar coordinate system is used in the analysis, with r, θ and z for radial, circumferential and axial directions respectively. Because of radial symmetry, no shear stresses exist over the section and σ_{rr} and $\sigma_{\theta\theta}$ are two lateral principal stresses. An unknown pressure p_1 can be assumed on the interface between the HSC core and ECC ring. On the interface, the radial stress σ_{rr} acting on both the HSC core and ECC ring equals to p_1. Meanwhile, there is no gap between HSC core and ECC ring, leading to the equal radial displacements on both sides of the interface.

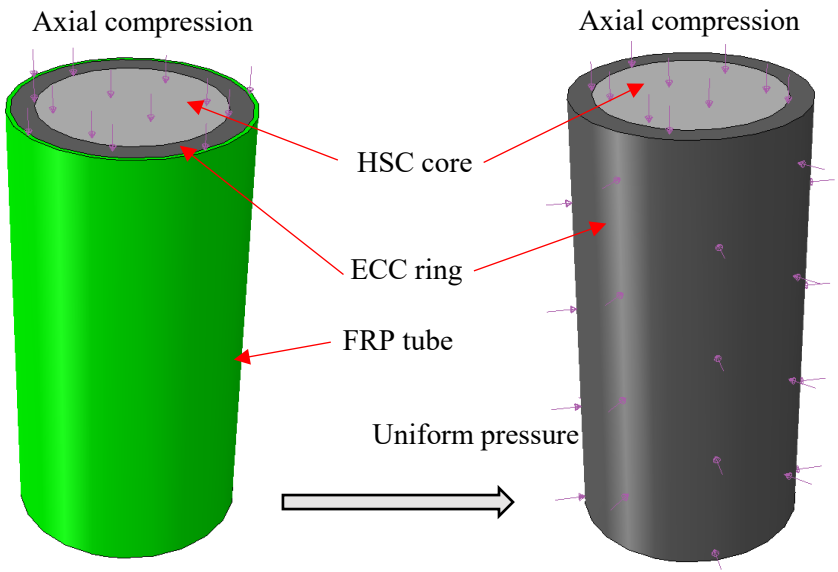

Fig. 1 FRP-ECC-HSC composite column under axial compression

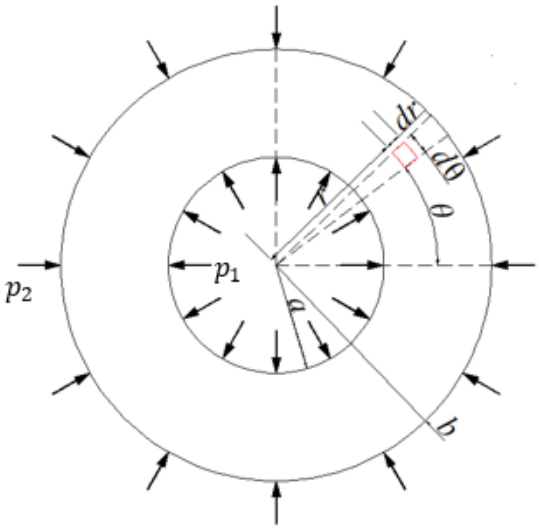

Fig. 2 Simplified calculation diagram of ECC ring

In the composite column, HSC core is under uniform confinement and the confining pressure equals to p_1 for the whole core section. For the ECC ring, it is subjected to outer pressure p_2 and inner pressure p_1. Fig. 2 shows the simplified calculation diagram of ECC ring, with the inner radius a and outer radius b.

One element, with the location of (r, θ, z), is chosen for the analysis. Equations of equilibrium, compatibility relations and stress-strain (constitutive) relations are adopted.

Equation of equilibrium in r direction:

$$\frac{\partial \sigma_{rr}}{\partial r} + \frac{1}{r}\frac{\partial \sigma_{\theta r}}{\partial \theta} + \frac{\partial \sigma_{zr}}{\partial z} + \frac{\sigma_{rr} - \sigma_{\theta\theta}}{r} + F_r = 0 \quad (1)$$

where stress components $\sigma_{\theta r} = \sigma_{zr} = 0$, body force $F_r = 0$, and Eq. (1) yields:

$$\sigma_{\theta\theta} - \sigma_{rr} = r\frac{\partial \sigma_{rr}}{\partial r} \quad (2)$$

$$\sigma_{\theta\theta} = \frac{d(r\sigma_{rr})}{dr} \quad (3)$$

Equation of geometric and strain compatibility relations:

$$\varepsilon_{rr} = \frac{\partial u}{\partial r}; \quad \varepsilon_{\theta\theta} = \frac{u}{r} \quad (4)$$

Based on Eq. (4), the following expression can be obtained:

$$\varepsilon_{rr} - \varepsilon_{\theta\theta} = r\frac{d\varepsilon_{\theta\theta}}{dr} \tag{5}$$

Since elastic material is considered here, linear stress-strain behavior can be expressed as:

$$\varepsilon_{rr} = \frac{1}{E}[\sigma_{rr} - \upsilon(\sigma_{\theta\theta} + \sigma_{zz})]; \quad \varepsilon_{\theta\theta} = \frac{1}{E}[\sigma_{\theta\theta} - \nu(\sigma_{rr} + \sigma_{zz})] \tag{6}$$

By substitution of Eq. (6) into Eq. (5), ε_{rr} and $\varepsilon_{\theta\theta}$ can be eliminated:

$$r\left(\frac{d\sigma_{\theta\theta}}{dr} - \nu\frac{d\sigma_{rr}}{dr}\right) = (1+\nu)(\sigma_{rr} - \sigma_{\theta\theta}) \tag{7}$$

By substitution of Eq. (3) into Eq. (7), the following expression can be obtained:

$$\frac{d(\sigma_{rr}+\sigma_{\theta\theta})}{dr} = 0 \tag{8}$$

which yields the result:

$$\sigma_{rr} + \sigma_{\theta\theta} = 2C \tag{9}$$

where $2C$ is a constant parameter. By substitution of Eq. (3) into Eq. (9) to eliminate $\sigma_{\theta\theta}$:

$$\frac{d(r\sigma_{rr})}{dr} + \sigma_{rr} = 2C \tag{10}$$

Multiply both sides of Eq. (10) by r:

$$r\frac{d(r\sigma_{rr})}{dr} + r\sigma_{rr} = \frac{d(r^2\sigma_{rr})}{dr} = 2Cr \tag{11}$$

Calculate the differential function and σ_{rr} and $\sigma_{\theta\theta}$ can be solved as follows:

$$\sigma_{rr} = \frac{A}{r^2} + C \qquad \sigma_{\theta\theta} = -\frac{A}{r^2} + C \tag{12}$$

The constants A and C can be determined by the boundary conditions $\sigma_{rr} = -p_1$ at $r = a$ and $\sigma_{rr} = -p_2$ at $r = b$. Then the lateral principal stresses over the ring section can be solved as:

$$\sigma_{rr} = \frac{a^2b^2(p_2-p_1)}{r^2(b^2-a^2)} + \frac{p_1a^2-p_2b^2}{b^2-a^2} \quad (13)$$

$$\sigma_{\theta\theta} = -\frac{a^2b^2(p_2-p_1)}{r^2(b^2-a^2)} + \frac{p_1a^2-p_2b^2}{b^2-a^2} \quad (14)$$

According to Eqs. (4), (6), (13) and (14), displacement in the radial direction can be solved as follows:

$$u = \frac{r}{E(b^2-a^2)}[(1-\nu)(p_1a^2 - p_2b^2) + \frac{(1+\nu)a^2b^2}{r^2}(p_1 - p_2) - (b^2 - a^2)\nu\sigma_{zz}] \quad (15)$$

For the ring section, the displacement at $r = a$ can be solved based on Eq. (15), with $E = E_o$ and $\nu = \nu_o$ representing the Young's modulus and Poisson's ratio of ECC:

$$u_{o,r=a} = \frac{a}{E_o(b^2-a^2)}[(1-\nu_o)(p_ia^2 - p_ob^2) + (1+\nu_o)b^2(p_i - p_o) - (b^2 - a^2)\nu_0E_o\varepsilon_{zz}] \quad (16)$$

where p_i is inner pressure and p_o is outer pressure applied on the ECC ring. ε_{zz} is axial shortening strain of the composite column.

For the core section, the radial displacement at $r = a$ can be solved as follows based on Eqs. (4) and (6):

$$u_{i,r=a} = \frac{a}{E_i}[-(1-\nu_i)p_i - \nu_iE_i\varepsilon_{zz}] \quad (17)$$

where p_i is the confining pressure applied on HSC core and equals to the inner pressure applied on the ECC ring. E_i and ν_i are the elastic modulus and Poisson's ratio of HSC core respectively.

There is no gap on the interface between the ring and core in the composite section, which leads to $u_{o,r=a} = u_{i,r=a}$. The pressure p_i can be calculated as:

$$p_i = \frac{2b^2\frac{E_i}{E_o}p_o + (\nu_o-\nu_i)(b^2-a^2)E_i\varepsilon_{zz}}{\frac{E_i}{E_o}(a^2+b^2) + (1+\nu_o\frac{E_i}{E_o}-\nu_i)(b^2-a^2)} \quad (18)$$

For FRP-ECC-HSC composite column, p_o is the outer pressure applied on the ECC ring, which is also the confining pressure provided by the FRP tube. It can be expressed as:

$$p_o = \sigma_l = \frac{E_f \varepsilon_f t_f}{R} \tag{19}$$

where R is the inner radius of FRP tube and equals to b for this case, E_f, ε_f, t_f are the Young's modulus, rupture strain and thickness of FRP tube respectively. For FRP-confined concrete of circular section, the hoop strain of FRP equals to the circumferential strain of the concrete element next to the FRP. Therefore, it yields the following equation:

$$\varepsilon_f = \varepsilon_{\theta\theta, r=b} \tag{20}$$

Based on Eqs. (4), (6), (15) (19) and (20), the following expression can be obtained:

$$p_o = \frac{E_f t_f}{b} \frac{1}{E_o(b^2 - a^2)} [(1 - \nu_o)(p_i a^2 - p_o b^2) + (1 + \nu_o) b^2 (p_i - p_o) - (b^2 - a^2) \nu_0 E_o \varepsilon_{zz}] \tag{21}$$

Using Eqs. (18) and (21), the confining pressure p_o applied on the ECC surface and the confining pressure p_i applied on the HSC core can be solved and expressed with the following functions:

$$p_o = f(E_i, E_o, \nu_i, \nu_o, \varepsilon_{zz}) \tag{22}$$

$$p_i = g(E_i, E_o, \nu_i, \nu_o, \varepsilon_{zz}) \tag{23}$$

In the FRP-EC-HSC composite column, elastic modulus of the ECC is much lower compared with that of HSC due to the absence of coarse aggregate. However, Poisson's ratio is nearly the same for these two cementitious materials. The tested Poisson's ratio was 0.21 for both HSC and ECC [5]. Therefore, Eq. (18) can be rewritten as:

$$p_i = \frac{2b^2 \frac{E_i}{E_o}}{\frac{E_i}{E_o}(a^2 + b^2) + (1 + \nu_o \frac{E_i}{E_o} - \nu_i)(b^2 - a^2)} p_o \tag{24}$$

in which it can be noted that the inner pressure p_i is independent on the axial compressive strain and is proportional to the outer pressure p_o. A parameter k is assigned as the transfer coefficient from the outer pressure to the inner pressure, considering the effect brought by the ECC ring in the composite column.

$$k = \frac{2b^2\frac{E_i}{E_o}}{\frac{E_i}{E_o}(a^2+b^2)+(1+\nu_o\frac{E_i}{E_o}-\nu_i)(b^2-a^2)} \tag{25}$$

It should be noted that for the concrete core, the confining pressure is uniformly distributed. Also, the radial stress and circumference stress are equal, which is the same as FRP-confined concrete cylinder. For the concrete ring, the two lateral stresses are not equal. Both radial stress and circumference stress at different locations over the ring section can be determined based on the above calculations, assuming the elastic material properties.

2.2 Transfer coefficient k

As shown in Eq. (25), it can be found that the coefficient k is related to Young's modulus and Poisson's ratio of the core and ring materials. In this present study, $\nu_o = \nu_i = 0.21$. Fig. 3 shows the variation of coefficient k with the change of Elastic Young's modulus ratio E_i/E_o, for different ratios of inner and outer ECC radius in the range of $a/b = 0.1 - 0.9$.

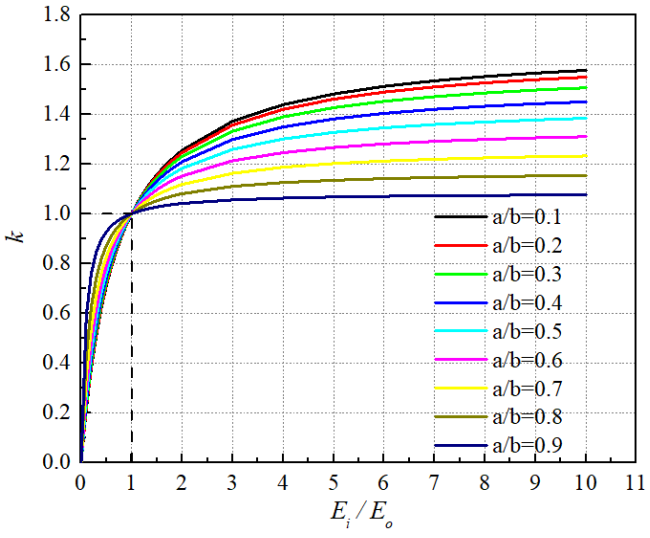

Fig. 3 Relation between coefficient k and Young's modulus ratio E_i/E_o

The following conditions can be observed and summarized:

(1) When $E_i > E_o$, $p_i > p_o$, it indicates that the confining pressure acting on the concrete core is larger than that provided by the confining FRP, if the concrete core has larger Elastic Young's modulus compared with the concrete ring. It can be found that the curve is approaching a constant value k_{max} with the increase of E_i/E_o for a certain a/b value. k_{max} is summarized in Table 2. Coefficient k is also related to the diameter ratio a/b, and the value of k_{max} increases with the decrease of a/b. It indicates that for a composite column of certain outer diameter and with certain confining material used, the thicker the ring section is, the larger the confining pressure will be produced and applied on the core section.

(2) When $E_i = E_o$, $p_i = p_o$, confining pressure is uniformly distributed over the whole column section, which is the same as FRP-confined one-grade concrete.

(3) When $E_i < E_o$, $p_i < p_o$, k will increase with the increase of a/b under a certain value of E_i/E_o, which is on the contrary to that when $E_i > E_o$.

Table 2 Value of k_{max} for different a/b

a/b	0.1	0.2	0.3	0.4	0.5	0.6	0.7	0.8	0.9
k_{max}	1.68	1.65	1.59	1.53	1.44	1.36	1.26	1.17	1.08

Table 3 Coefficient k for FRP-ECC-HSC specimens

ID	ECC ratio	E_i/E_o	k
FE50H70-15	0.278	2.09	1.06
FE50H70-25	0.438	2.09	1.10
FE50H90-15	0.278	2.31	1.07
FE50H90-25	0.438	2.31	1.11

For the FRP-ECC-HSC composite column, elastic modulus of HSC core is larger than that of ECC ring. Therefore, the confining pressure applied on HSC core is larger compared with that provided by the FRP tube. Transfer coefficient k, which can also be regarded as the confining pressure enhancement ratio, is listed in Table 3 for the investigated FRP-ECC-HSC specimens. ECC ratio α can be defined as the ratio of ECC ring area over the confined concrete area as follows:

$$\alpha = {A_e}/{A_c} = {A_e}/{(A_h + A_e)} \tag{26}$$

where A_e, A_h and A_c represent the sectional areas of ECC ring, HSC core and the whole confined concrete. It can be observed that the value k is similar for specimens with C70 and C90 as HSC core, due to insignificant difference on the elastic modulus. k will increase with the increase of ECC ratio. The confining pressure applied on HSC core is enhanced by around 6% and 10% respectively, for specimens with ECC thickness of 15 mm and 25 mm.

3. Analysis-oriented model for FRP-confined concrete

Existing analysis-oriented models can give predictions on the stress-strain behavior of concrete under uniform confinement, such as the FRP-confined circular solid concrete. For the FRP-ECC-HSC composite column, however, the analysis models cannot provide direct predictions since the ECC ring is under non-uniform confinement, with the confining pressure varying at different locations. Therefore, finite element (FE) modeling is used to simulate the compressive behavior of FRP-ECC-HSC composite columns. Accurate elastic-plastic material properties for confined concrete are needed to input into the FE models. Analysis-oriented models, which are presented in this section, are used to generate the input material data.

3.1 FRP-confined HSC

The basic concept of analysis-oriented models for FRP-confined concrete is using equations to describe the interaction of the following four parameters under uniform confinement: axial strain ε_c, axial stress σ_c, lateral strain ε_l and lateral stress σ_l. Compared with design-oriented models which can give predictions on the ultimate compressive strength and strain with closed form empirical equations, analysis-oriented models provide predictions on the whole stress-strain curve of confined concrete, which are more theoretically based and versatile. Three relationships are included in analysis-oriented models: (1) axial stress-axial strain ($\sigma_c - \varepsilon_c$) relations under certain confining pressures; (2) lateral strain-axial strain ($\varepsilon_l - \varepsilon_c$) relations and (3) lateral stress-lateral strain ($\sigma_l - \varepsilon_l$) relations. For uniformly confined concrete (circular sections), lateral stress σ_l in concrete is equal to the confining pressure f_l provided by the confining material. Based on the equilibrium condition, σ_l or f_l can be calculated using Eq. (19).

Extensive equations for $\sigma_c - \varepsilon_c$ relations of concrete under certain confining pressure have been proposed in the literature [27,28]. They are also termed as actively-confined models, since the confining pressure is independent with the loading process. By contrast, FRP-confined concrete is termed as passively-confined, with the confining pressure increasing linearly with the increase of lateral strain (as the relationship presented in Eq. (19)). Most of the analysis-oriented models assume that the axial stress for FRP-confined concrete is the same as that for actively-confined concrete under the same axial strain and lateral strain. However, some research figured out this assumption is not correct, since the axial stress for FRP-confined concrete is found to be lower than that for actively-confined concrete under the same axial strain, especially for high strength concrete. Lim and Ozbakkaloglu [7] proposed an approach to consider this path-dependence behavior. Reduced confining pressures are adopted in $\sigma_c - \varepsilon_c$ relations, so that the axial stress obtained from actively-confined models is closer to the actual axial stress of FRP-confined concrete. The reducing value of confining pressure is

generated by empirical equations [29]. This approach is validated against a large test database, which consists of large amount of high strength concrete data especially. Therefore, it is adopted in this study for the confined HSC core in the FRP-ECC-HSC composite column. Detailed information can refer to Lim and Ozbakkaloglu [7].

Hoop strain-axial strain relationship ($\varepsilon_l - \varepsilon_c$) reflects the dilation behavior and has direct influence on the confining pressure for FRP-confined concrete. Fig. 4 presents the comparison of hoop strain-axial strain curves between test results of FH70 and FH90 specimens and the corresponding predictions by the existing models [27,30,31]. It shows that Lim and Ozbakkaloglu's model [30], with the expression as shown in Eq. (27), could provide the closest predictions overall in terms of the curve shape.

$$\varepsilon_c = \frac{\varepsilon_l}{v\left[1+\left(\frac{\varepsilon_l}{v\varepsilon_{c0}}\right)^{1+0.03f'_{c0}}\right]^{1/(1+0.03f'_{c0})}} + 0.04{\varepsilon_l}^{0.7}\left[1+\mathbf{21}\left(\frac{f_l}{f'_{c0}}\right)^{\mathbf{0.8}}\right] \quad (27)$$

where v is Poisson's ratio of concrete; f'_{c0} and ε_{c0} are compressive strength and the corresponding strain of unconfined concrete.

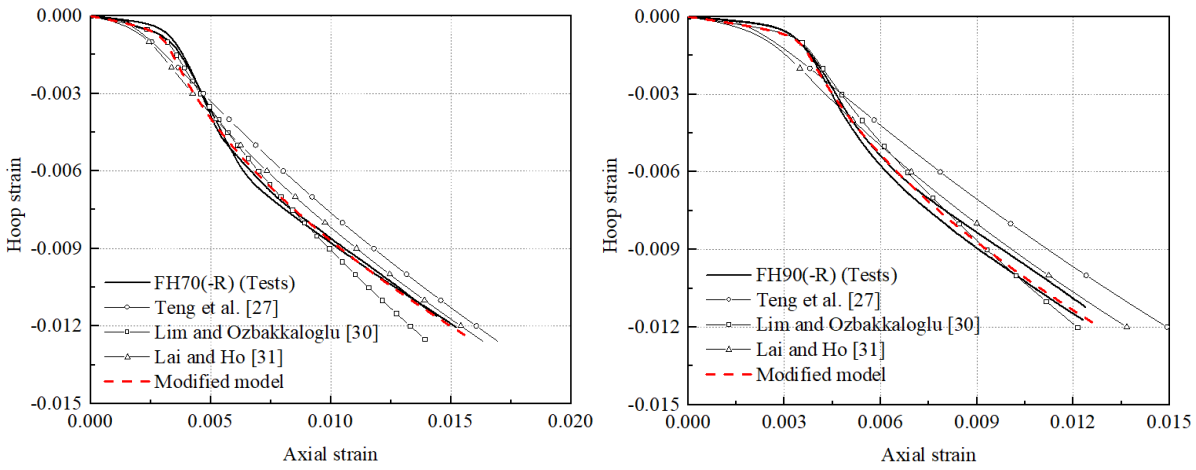

(a) FH70 specimens (b) FH90 specimens

Fig. 4 Comparisons of hoop strain-axial strain behavior between test results and predictions for FRP-confined HSC

292 However, the slope of the curve for the strain hardening stage is still not in line with each other
293 between the test results and Lim and Ozbakkaolglu's model predictions. This difference will
294 also lead to inconsistency of the axial stress-axial strain behavior. It is found that the coefficient
295 21 and index 0.8 in Eq. (27) have large influence on the slope of the curve. In order to describe
296 the hoop strain-axial strain behavior of FRP-confined HSC more accurately, modified equation
297 based on Lim and Ozbakkaloglu's model could be proposed as Eq. (28):

298 $$\varepsilon_c = \frac{\varepsilon_l}{v\left[1+\left(\frac{\varepsilon_l}{v\varepsilon_{c0}}\right)^{1+0.03f'_{c0}}\right]^{1/(1+0.03f'_{c0})}} + 0.04{\varepsilon_l}^{0.7}\left[1 + \boldsymbol{A}\left(\frac{f_l}{f'_{c0}}\right)^{\boldsymbol{B}}\right] \quad (28)$$

299 where A and B are the two parameters needed to be modified. It should be noted that Eq. (27)
300 was developed using the large database consisting of both normal strength concrete and high
301 strength concrete confined by different types of FRP, such as Carbon FRP (CFRP), Aramid
302 FRP (AFRP) and Glass FRP (GFRP). Meanwhile, both FRP wrap confined concrete and FRP
303 tube confined concrete were considered [30]. Therefore, it may lead to the reason that Eq. (27)
304 could not give the best predictions to the test results of FH70 and FH90, which are high strength
305 concrete confined by GFRP tube.

306 To calibrate parameters A and B, additional test data of GFRP tube-confined HSC were
307 collected from the literature and listed in Table 4 [32,33]. All the specimens included have the
308 normal diameter of 200 mm with the unconfined concrete strength ranging from 54.1 MPa to
309 104.4 MPa. By analysing the test data, it is found that the hoop strain-axial strain relation is
310 also associated with confining stiffness K_l, which can be expressed as:

311 $$K_l = \frac{2E_f t_f}{D} \quad (29)$$

312 where E_f and t_f are the Young's modulus and thickness of FRP tube, and D is the diameter of
313 the confined concrete. The parameter A is linearly correlated with K_l (unit in MPa) as follows:

$$A = 49 - 0.0034K_l \quad (30)$$

B is assigned as 1.13 to best fit the test data. With this modified model, ultimate axial strain corresponding to the actual hoop rupture strain can be calculated as well and are listed in Table 5 for the collected test data. Close agreement between the test results and the predicted results by the modified model can be obtained as shown in Fig. 5. Meanwhile, predictions of ultimate axial strain calculated by the existing models are also presented in Table 5 and Fig. 5. Satisfactory behavior of the newly modified model can be observed through the comparison. It is worth noting that Lai and Ho's model [31] could also provide good predictions on the ultimate axial strain in terms of the values of mean and coefficient of variation. However, its predictions are not consistent with the test results for the initial part of the hoop strain-axial strain curve as presented in Fig. 4. Therefore, the modified model, instead of Lai and Ho's model [31], is adopted in this study.

326

Table 4 Test data for HSC filled GFRP tube

Source	Specimen label	Concrete		GFRP tube			Test results		
		f'_{c0} (MPa)	ε_{c0}	E_c (GPa)	E_f (GPa)	t_f (mm)	f'_{cc} (MPa)	$\varepsilon_{h,rup}$	ε_{cc}
Li et al. [5]	FH70	75.4	0.0028	32	39.8	2.5	82.1	0.0116	0.0144
	FH70-R	75.4	0.0028	32	39.8	2.5	84.3	0.0121	0.0152
	FH90	96.8	0.0032	35.3	39.8	2.5	94.0	0.0117	0.0123
	FH90-R	96.8	0.0032	35.3	39.8	2.5	94.2	0.0112	0.0124
Zhang et al. [32]	S54-2FW-M	54.1	0.0025	27.8	45.9	2.2	101.3	0.0143	0.0225
	S54-2FWC1	54.1	0.0025	27.8	45.9	2.2	86.0	0.0108	0.0176
	S54-2FWC1	54.1	0.0025	27.8	45.9	2.2	88.7	0.0111	0.0189
	S84-4FW-M	84.6	0.0027	33.1	45.9	4.7	156.1	0.0117	0.0220
	S84-4FW-C	84.6	0.0027	33.1	45.9	4.7	152.3	0.0110	0.0239
	S84-9FW-M	84.6	0.0027	33.1	45.9	9.5	236.2	0.0112	0.0317
	S84-9FW-C	84.6	0.0027	33.1	45.9	9.5	236.2	0.0105	0.0322
	S104-4FW-M	104.4	0.0031	36.5	45.9	4.7	188.8	0.0119	0.0264
	S104-4FW-M	104.4	0.0031	36.5	45.9	4.7	179.6	0.0132	0.0258
	S104-4FW-M	104.4	0.0031	36.5	45.9	4.7	167.6	0.0109	0.0238
Zhang et al. [33]	C59-F80-T4-1	58.8	0.0027	36.3	36.2	4	115.3	0.0113	0.0213
	C59-F80-T4-2	58.8	0.0027	36.3	36.2	4	113.0	0.0121	0.0205
	C59-F80-T6-1	58.8	0.0027	36.3	36.2	6	158.2	0.0120	0.0281

	C59-F80-T6-2	58.8	0.0027	36.3	36.2	6	153.5	0.0120	0.0287
	C80-F80-T4-1	80.2	0.003	42.4	36.2	4	126.8	0.0103	0.0146
	C80-F80-T4-2	80.2	0.003	42.4	36.2	4	135.1	0.0098	0.0170
	C80-F80-T6-1	80.2	0.003	42.4	36.2	6	180.7	0.0120	0.0239
	C80-F80-T6-2	80.2	0.003	42.4	36.2	6	171.7	0.0120	0.0251

327

328 Table 5 Predictions on ultimate axial strain ε_{cc} by different models

Source	Specimen label	Test results	Predictions by Teng et al. [27]		Predictions by Lim and Ozbakkaloglu [30]		Predictions by Lai and Ho [31]		Predictions by the modified model	
		$\varepsilon_{cc,test}$	$\varepsilon_{cc,pre}$	$\frac{\varepsilon_{cc,pre}}{\varepsilon_{cc,test}}$	$\varepsilon_{cc,pre}$	$\frac{\varepsilon_{cc,pre}}{\varepsilon_{cc,test}}$	$\varepsilon_{cc,pre}$	$\frac{\varepsilon_{cc,pre}}{\varepsilon_{cc,test}}$	$\varepsilon_{cc,pre}$	$\frac{\varepsilon_{cc,pre}}{\varepsilon_{cc,test}}$
Li et al. [5]	FH70	0.0144	0.0155	1.07	0.0128	0.89	0.0148	1.03	0.0142	0.99
	FH70-R	0.0152	0.0162	1.07	0.0134	0.88	0.0156	1.02	0.0150	0.99
	FH90	0.0123	0.0145	1.18	0.0118	0.96	0.0133	1.08	0.0124	1.01
	FH90-R	0.0124	0.0139	1.12	0.0113	0.91	0.0127	1.02	0.0118	0.95
Zhang et al. [32]	S54-2FW-M	0.0225	0.0235	1.04	0.0195	0.87	0.0240	1.07	0.0255	1.13
	S54-2FWC1	0.0176	0.0166	0.94	0.0140	0.79	0.0166	0.94	0.0167	0.95
	S54-2FWC1	0.0189	0.0171	0.91	0.0144	0.76	0.0172	0.91	0.0174	0.92
	S84-4FW-M	0.0220	0.0233	1.06	0.0187	0.85	0.0224	1.02	0.0233	1.06
	S84-4FW-C	0.0239	0.0215	0.91	0.0173	0.73	0.0206	0.86	0.0212	0.89

	S84-9FW-M	0.0317	0.0377	1.19	0.0278	0.88	0.0360	1.13	0.0360	1.14
	S84-9FW-C	0.0322	0.0345	1.07	0.0255	0.79	0.0327	1.01	0.0324	1.01
	S104-4FW-M	0.0264	0.0219	0.83	0.0172	0.65	0.0199	0.75	0.0202	0.77
	S104-4FW-M	0.0258	0.0249	0.96	0.0194	0.75	0.0229	0.89	0.0236	0.91
	S104-4FW-M	0.0238	0.0197	0.83	0.0156	0.65	0.0178	0.75	0.0179	0.75
Zhang et al. [33]	C59-F80-T4-1	0.0213	0.0218	1.02	0.0176	0.82	0.0212	1.00	0.0224	1.05
	C59-F80-T4-2	0.0205	0.0237	1.16	0.0191	0.93	0.0233	1.14	0.0249	1.22
	C59-F80-T6-1	0.0281	0.0318	1.13	0.0244	0.87	0.0311	1.11	0.0345	1.23
	C59-F80-T6-2	0.0287	0.0318	1.11	0.0244	0.85	0.0311	1.08	0.0345	1.20
	C80-F80-T4-1	0.0146	0.0184	1.26	0.0147	1.01	0.0169	1.16	0.0153	1.05
	C80-F80-T4-2	0.0170	0.0174	1.02	0.0139	0.82	0.0159	0.94	0.0143	0.84
	C80-F80-T6-1	0.0239	0.0263	1.10	0.0203	0.85	0.0245	1.03	0.0259	1.09
	C80-F80-T6-2	0.0251	0.0263	1.05	0.0203	0.81	0.0245	0.98	0.0259	1.03
	Mean			1.05		0.83		1.00		1.01
	Cov			0.106		0.104		0.111		0.127

329

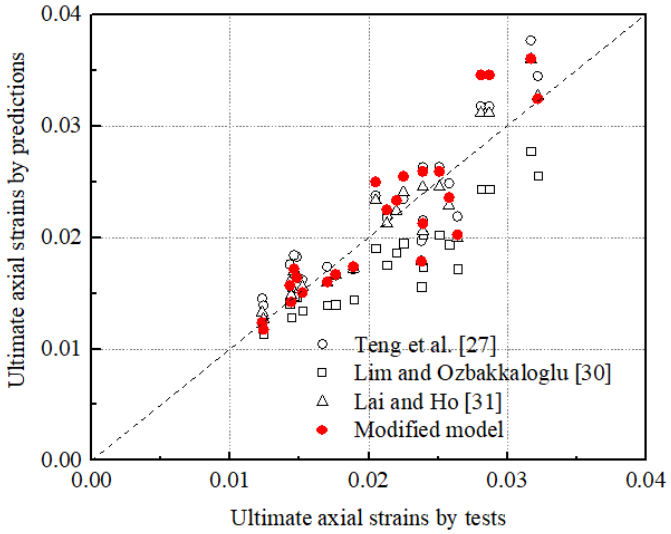

330

331 Fig. 5 Comparison of ultimate axial strain between predictions and test results

332 Hoop strain-axial strain ($\varepsilon_l - \varepsilon_c$) curves generated with the modified model is plotted in Fig.
333 4 for the comparison with test curves of FH70 and FH90 specimens. It shows that enhanced
334 agreements with the test results can be obtained compared with the original model and other
335 existing models. It is noted that the comparisons of the hoop strain-axial strain curve between
336 the modified model predictions and test results are not presented for the additional collected
337 data [32,33] in Fig. 4, since the whole hoop strain-axial strain curves were not reported in the
338 corresponding paper.

339 The modified $\varepsilon_l - \varepsilon_c$ equation is used together with the actively-confined model proposed by
340 Lim and Ozbakkaloglu [7] and the $\sigma_l - \varepsilon_l$ relationship presented in Eq. (19) to form the newly
341 proposed analysis-oriented model for FRP-confined HSC core in this study. The axial stress-
342 axial strain curves for FH70 and FH90 specimens are shown in Fig. 6. Close agreements can
343 be obtained between the test results and predictions by the modified analysis-oriented model.
344 Furthermore, it can be seen that the accurate model for hoop strain-axial strain relation is of
345 vital importance for the prediction of axial stress-axial strain behavior of FRP-confined
346 concrete. This modified analysis-oriented model will be used to generate the material data for
347 confined HSC in ABAQUS [34] to simulate the behavior of FRP-ECC-HSC specimens.

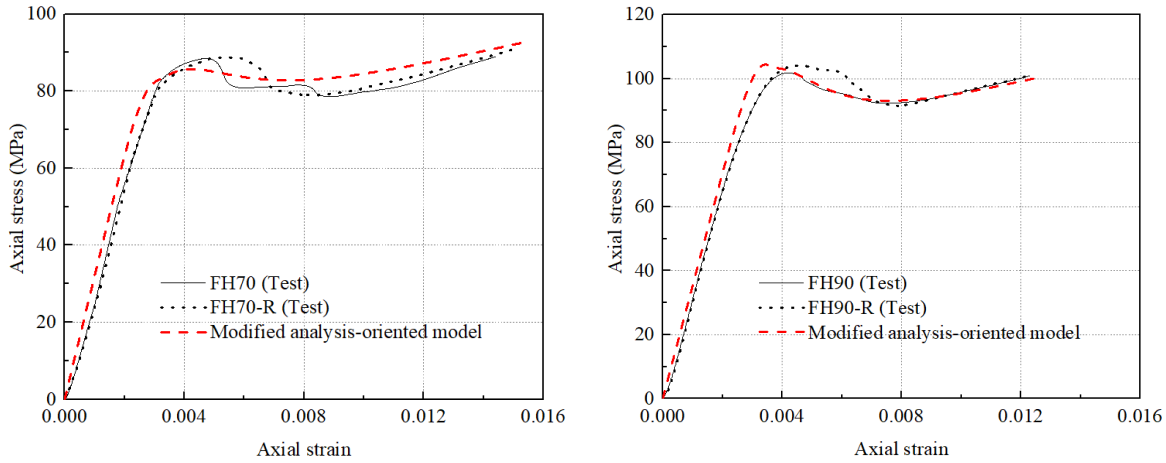

(a) FH70 specimens (b) FH90 specimens

Fig. 6 Predictions of axial stress-axial strain behavior for FRP-confined HSC specimens

3.2 FRP-confined ECC

Compared with normal concrete, FRP-confined ECC has not been widely investigated in the existing research. It is noted that the dilation behavior of confined ECC is obviously different from that of confined normal concrete because of the self-confinement effect. Therefore, the existing analysis-oriented models for FRP-confined normal concrete is not applicable to FRP-confined ECC. Based on the existing research and test data, a new analysis-oriented model is proposed and validated in this section.

Similar to FRP-confined normal concrete, the general approach uses the three relationships discussed in section 3.1, with the lateral stress-lateral strain ($\sigma_l - \varepsilon_l$) relation remains unchanged for uniformly confined ECC as shown in Eq. (19). Popovic's model is used to generate the axial stress-axial strain ($\sigma_c - \varepsilon_c$) relations under certain confining pressures [28]. The equation is expressed as follows:

$$\sigma_c = \frac{f_{cc}'^{*}(\varepsilon_c/\varepsilon_{cc}^{*})r}{r-1+(\varepsilon_c/\varepsilon_{cc}^{*})^r} \tag{31}$$

in which the parameter r is defined as:

$$r = \frac{E_c}{E_c - f'^{*}_{cc}/\varepsilon^{*}_{cc}} \tag{32}$$

E_c is the elastic modulus of concrete; f'^{*}_{cc} and ε^{*}_{cc} are the compressive strength and the corresponding compressive strain of confined concrete under the confining pressure f_l. Li et al. [22] conducted experimental investigations on ECC cylinders under triaxial compression and developed the following expressions for f'^{*}_{cc} and ε^{*}_{cc}:

$$f'^{*}_{cc} = f'_{c0} + 2.866 f_l \tag{33}$$

$$\varepsilon^{*}_{cc} = \varepsilon_{c0}\left(1 + 7.399 \frac{f_l}{f'_{c0}}\right) \tag{34}$$

Eqs. (33) and (34) are adopted together with Eqs. (31) and (32) to form the actively-confined model for FRP-confined ECC to generate the axial stress-axial strain ($\sigma_c - \varepsilon_c$) relations under certain confining pressures. Compared with the model proposed by Jiang and Teng [6] for FRP-confined normal concrete, the strength enhancement coefficient 3.5 is replaced with 2.866 in Eq. (33) and the strain enhancement coefficient 17.5 is replaced with 7.399 in Eq. (34). This is related to the different compressive properties between normal concrete and ECC [23,24].

The equation proposed by Yuan et al. [24] is adopted in this study to determine the hoop strain-axial strain ($\varepsilon_l - \varepsilon_c$) behavior for FRP-confined ECC, which is expressed as follows:

$$\varepsilon_c = \varepsilon_{c0}\left(1 + 8 f_l / f'_{c0}\right)\left[1.015\left(\varepsilon_l/\varepsilon_{c0}\right)^{0.305} + 0.221\left(\varepsilon_l/\varepsilon_{c0}\right)\right] \tag{35}$$

Comparisons between predictions by Eq. (35) and test results are presented in Fig. 7 for different ECC strengths and confining stiffnesses, which exhibit close agreements. As anticipated, with the increase of confining stiffness, hoop strain will increase more slowly because of the stronger confinement. It is worth noting that the inconsistence of the test data with compressive strength of 64.6 MPa and confining stiffness of 2463.3 MPa can be observed as shown in Fig. 7(b). It presents a faster development of the hoop strain compared with the

test data with a lower confining stiffness of 1539.6 MPa, which is abnormal. Therefore, the prediction obtained by Eq. (35) cannot match well with this data. This presented test data in [23] may require further examination.

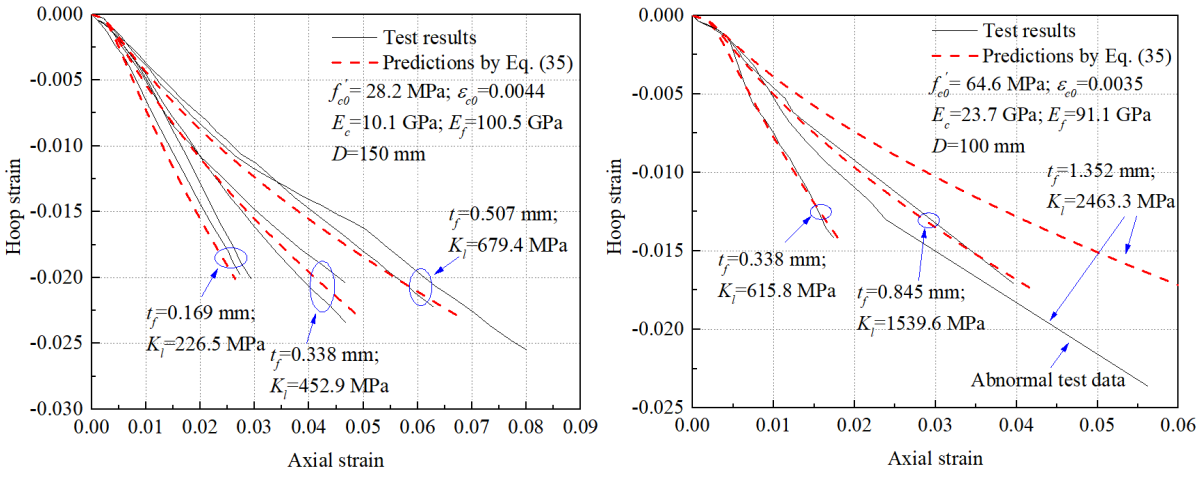

(a) Test data adopted from [24] (b) Test data adopted from [23]

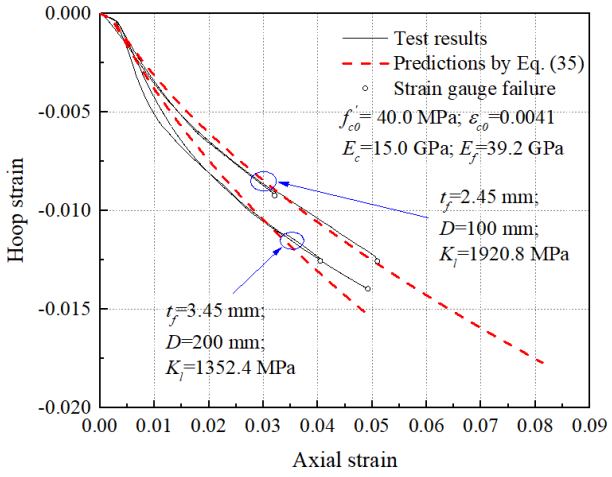

(c) Test data by the authors

Fig. 7 Comparisons of hoop strain-axial strain behavior between test results and predictions for FRP-confined ECC

Three relationships for the proposed analysis-oriented model of FRP-confined ECC are clearly presented in Eqs. (19, 31-35). Axial stress-axial strain behavior is predicted and compared with test results in Fig. 8. Similar to FRP-confined normal concrete, the enhancement ratio of both

399 compressive strength and ultimate compressive strain will be increased with the increase of
400 confining stiffness for FRP-confined ECC. Close agreements can be obtained for the group of
401 data with ECC strength of 28.2 MPa as shown in Fig 8(a), indicating the good performance of
402 the proposed analysis-oriented model. For another group of data, however, the predictions
403 present relatively larger deviations as shown in Fig. 8(b). This group of test data in [23] may
404 require further examination.

405 To further validate the proposed analysis-oriented model, four FRP-confined ECC stub
406 columns were prepared and axially compressed by the authors. Similar to the FRP-ECC-HSC
407 composite columns investigated in this study, the newly tested specimens are also FRP tube
408 confined concrete. Test arrangements, including the specimen size, test setup and
409 instrumentations, are similar to those in [23] and [24]. Two different nominal sectional
410 diameters, 100 mm and 200 mm, were considered for the stub column, while the corresponding
411 nominal heights were 200 mm and 400 mm, respectively. Material properties of ECC and FRP
412 are summarized in Figs. 7(c) and 8(c). Hoop strain-axial strain curves and axial stress-axial
413 strain curves are presented in Figs. 7(c) and 8(c). It can be observed that the predictions could
414 match well with the test results, indicting the applicability of the proposed analysis-oriented
415 model in the scope of the current study.

416 It is worth noting that Eqs. (33-35) in the proposed analysis-oriented model are adopted from
417 the existing studies for confined ECC and validated based on the limited available test data.
418 More tests are needed to further validate the applicability of the proposed model for a broader
419 range in future studies. The proposed analysis-oriented model will be used to generate the
420 material data for confined ECC in ABAQUS [34] to simulate the behavior of FRP-ECC-HSC
421 composite column under axial compression. Good agreements between test results and FE
422 results are obtained and presented in section 4. It also demonstrates that this proposed analysis-
423 oriented model for FRP-confined ECC is applicable to this study.

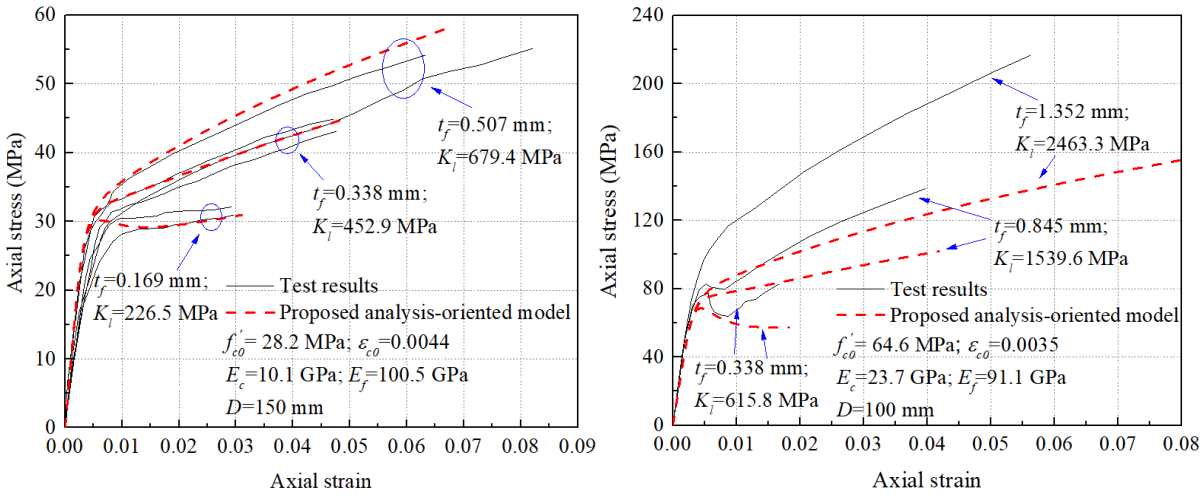

(a) Test data adopted from [24] (b) Test data adopted from [23]

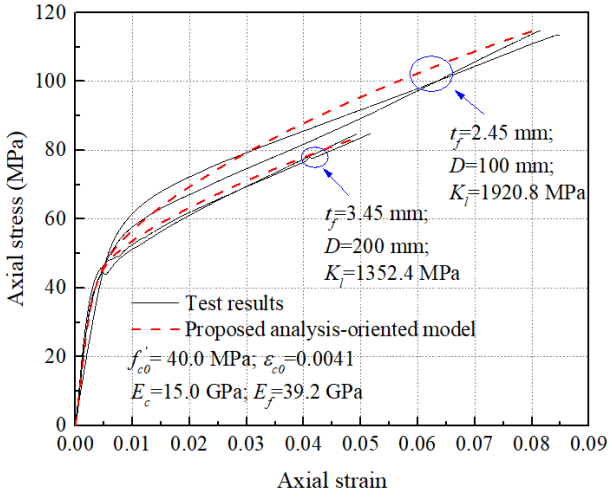

(c) Test data by the authors

Fig. 8 Comparisons of axial stress-axial strain behavior between test results and predictions for FRP-confined ECC

4. Finite element modeling

4.1 CDP implementation

Concrete damaged plasticity (CDP) model is adopted to simulate the axial compressive behavior of confined concrete. It is noted that either damage or plasticity can describe the

435 nonlinear behavior of concrete [35]. Yu et al. [16] used pure plasticity to determine the strain
436 hardening behavior before the peak stress, while assuming perfectly-plastic behavior after the
437 peak stress, in which the yield surface was set to be unchanged and only damage was defined
438 to determine the strain softening behavior of concrete. On the other hand, it is also well
439 accepted that damage could be defined to characterise the degraded elastic modulus of concrete
440 during the unloading path in cyclic compression. Since only monotonic compression is
441 involved in this study, it is reasonable to use plasticity only to describe the strain hardening
442 behavior before peak stress and the strain softening behavior after peak stress, while no damage
443 is defined.

444 For CDP model implemented in ABAQUS frame [34], yield function proposed by Lubliner et
445 al. [36] and further developed by Lee and Fenves [37] is adopted to describe the evolution of
446 concrete under compression. The yield function F is expressed as follows:

447 $$F = \frac{1}{1-\alpha}\left(\bar{q} - 3\alpha\bar{p} + \beta\left(\bar{\varepsilon}_p\right)\langle -\bar{\sigma}_{min}\rangle - \gamma\langle\bar{\sigma}_{min}\rangle\right) - \bar{\sigma}_c\left(\bar{\varepsilon}_{pc}\right) = 0 \quad (36)$$

448 $$\alpha = \frac{f_b'/f_{c0}' - 1}{2f_b'/f_{c0}' - 1};\ 0 \le \alpha \le 0.5 \quad (37)$$

449 $$\beta = \frac{\bar{\sigma}_c\left(\bar{\varepsilon}_{pc}\right)}{\bar{\sigma}_t\left(\bar{\varepsilon}_{pt}\right)}(1-\alpha) - (1-\alpha) \quad (38)$$

450 $$\gamma = \frac{3(1-K)}{2K-1} \quad (39)$$

451 where $\bar{p}$ and $\bar{q}$ are equivalent effective pressure and von Mises equivalent effective stress,
452 which can be expressed as

453 $$\bar{p} = \frac{1}{3}(\bar{\sigma}_1 + \bar{\sigma}_2 + \bar{\sigma}_3) \quad (40)$$

454 $$\bar{q} = \sqrt{3\frac{(\bar{\sigma}_1 - \bar{\sigma}_2)^2 + (\bar{\sigma}_2 - \bar{\sigma}_3)^2 + (\bar{\sigma}_3 - \bar{\sigma}_1)^2}{6}} \quad (41)$$

f_b'/f_{c0}' is the ratio of biaxial compressive strength to uniaxial compressive strength and is suggested that $f_b'/f_{c0}' = 1.57f_{c0}'^{-0.09}$ [38]. K is the ratio of the second stress invariant on the tensile meridian to that on the compressive meridian and is suggested to be $0.71f_{c0}'^{-0.025}$ [38]. $\bar{\sigma}_c$ and $\bar{\sigma}_t$ are the effective compressive and tensile cohesion stresses. $\bar{\varepsilon}_{pc}$ and $\bar{\varepsilon}_{pt}$ are the equivalent compressive and tensile plastic strains. $\bar{\sigma}_{min}$ is the minimum principle effective stress. For concrete under triaxial compression, compressive stresses are assigned to be positive, leading to $\langle -\bar{\sigma}_{min} \rangle = 0$, while $\langle \bar{\sigma}_{min} \rangle = \bar{p} - \frac{1}{3}\bar{q}$. Therefore, Eq. (36) yields the following expression:

$$\bar{\sigma}_c(\bar{\varepsilon}_{pc}) = \frac{3+\gamma}{3(1-\alpha)}\bar{q} - \frac{3\alpha+\gamma}{1-\alpha}\bar{p} \tag{42}$$

For uniformly FRP-confined concrete, Eq. (40) and (41) can be rewritten as:

$$\bar{p} = \frac{1}{3}(2\sigma_l + \sigma_c) \tag{43}$$

$$\bar{q} = \sigma_c - \sigma_l \tag{44}$$

Substituting Eqs. (43) and (44) into Eq. (42), it yields the following expression:

$$\bar{\sigma}_c(\bar{\varepsilon}_{pc}) = \sigma_c - \frac{1+2\alpha+\gamma}{1-\alpha}\sigma_l \tag{45}$$

Based on Eq. (45), equivalent compressive cohesion stress can be calculated under different confining pressures and input as the yield stress data in ABAQUS [34], which is also understood as the hardening/softening rule in CDP model for FRP-confined concrete under monotonic compression.

CDP model adopts non-associated flow rule to consider the plastic development behavior of concrete. As suggested by the previous research [38,39], dilation angle φ is calculated with the following expression:

476 $$tan\varphi = -\frac{3(d\varepsilon_{c,p}+2d\varepsilon_{l,p})}{2(d\varepsilon_{c,p}-d\varepsilon_{l,p})} \quad (46)$$

477 in which $\varepsilon_{c,p}$ and $\varepsilon_{l,p}$ are axial and lateral plastic strain, and can be expressed as:

478 $$\varepsilon_{c,p} = \varepsilon_c - \frac{1}{E_c}(\sigma_c - 2v\sigma_l) \quad (47)$$

479 $$\varepsilon_{l,p} = \varepsilon_l + \frac{1}{E_c}[(1-v)\sigma_l - v\sigma_c] \quad (48)$$

480 For concrete under non-uniform confinement, that the two lateral principal stresses σ_2 and σ_3
481 are not equal, Yu et al. [16] suggested to use the following equation to calculate the equivalent
482 confining pressure $\sigma_{l,eq}$:

483 $$\sigma_{l,eq} = \frac{2(\sigma_2+af'_{c0})(\sigma_3+af'_{c0})}{(\sigma_2+\sigma_3+2af'_{c0})} - af'_{c0} \quad (49)$$

484 in which the parameter a is calibrated to be 0.039 to best fit the test results [40]. Similarly,
485 equivalent lateral strain of the ring region can be expressed using the similar equation as
486 follows:

487 $$\varepsilon_{l,eq} = \frac{2(\varepsilon_2+a\varepsilon_{c0})(\varepsilon_3+a\varepsilon_{c0})}{(\varepsilon_2+\varepsilon_3+2a\varepsilon_{c0})} - a\varepsilon_{c0} \quad (50)$$

488 Therefore, the equivalent confining stiffness of the non-uniformly confined concrete in the ring
489 region can be calculated together with Eqs. (49,50):

490 $$K_{l,eq} = \frac{\sigma_{l,eq}}{\varepsilon_{l,eq}} \quad (51)$$

491 It is noted that for FRP-confined concrete, hardening/softening rule is related to confining
492 pressure, while the flow rule is related to axial plastic strain and confining stiffness [16]. Five
493 field variables of axial plastic strain, confining pressure and confining stiffness are defined
494 with user subroutine in ABAQUS [34]. Field variable 1 is defined as the axial plastic strain and
495 is associated with the flow rule of HSC and ECC; field variables 2 and 4 are defined as the

confining pressure and are associated with the hardening/softening rule of HSC and ECC, respectively; field variables 3 and 5 are defined as the confining stiffness and are associated with the flow rule of HSC and ECC, respectively. Detailed information of the implementing procedure can refer to Yu et al. [16].

4.2 FE model and validation

In this section, test results on FRP-confined HSC specimens and FRP-ECC-HSC specimens obtained by the authors [5] are used to validate the developed FE models. Information for the test specimens is shown in Table 1. In the test, FRP-ECC-HSC composite columns were restrained by the top and bottom loading plate when subjected to axial compression. However, the constraints are considered to have limited effects on the compressive behavior of FRP-confined concrete, especially for the mid-height region of the column [16]. In this study, therefore, only a quarter of sliced model with 10 mm thickness was established for the composite column behavior simulation, as shown in Fig. 9. 8-node solid elements were used to model the concrete part, including HSC core and ECC ring. Membrane elements were used for the FRP tube. Symmetry boundary conditions were applied on the model. Axial displacement loading was applied on the top surface, while axial displacement constraint was applied on the bottom surface to simulate the axial shortening of the column. It is assumed that there is no slip among the different components in the composite column under axial compression, so that "Tie" option was used to model the interaction behavior between HSC core and ECC ring as well as ECC ring and FRP tube.

Before the validation of FRP-ECC-HSC composite column, uniformly FRP-confined HSC and FRP-confined ECC are firstly validated, as shown in Fig. 10. FE results could replicate the results obtained by the analysis-oriented models presented in section 3, which indicates that the implementation of CDP model in ABAQUS [34] and the subroutine used are appropriate.

Fig. 11 shows the typical axial stress distribution of FRP-ECC-HSC composite column section, with the example of the specimen FE50H90-25. It can be clearly observed that the axial stress for different elements of HSC core is the same, which means the HSC core is under uniform confinement in the composite column. For ECC ring, however, it is subjected to non-uniform confinement, leading to different axial stresses at different locations. Hoop strain-axial strain behavior and axial stress-axial strain behavior are plotted in Fig. 12 and Fig. 13, respectively. Close agreements between test results and FE results can be obtained, indicating that the proposed FE model could simulate the axial compressive behavior of FRP-ECC-HSC composite column accurately. Ultimate axial load and ultimate axial compressive strain for all the specimens obtained by FE simulation are summarized and compared with test results in Table. 6. It should be noted that all the ultimate conditions of the FE simulation are governed by FRP rupture, in which the FRP rupture strains are calculated by averaging the hoop rupture strains of the corresponding two identical test specimens.

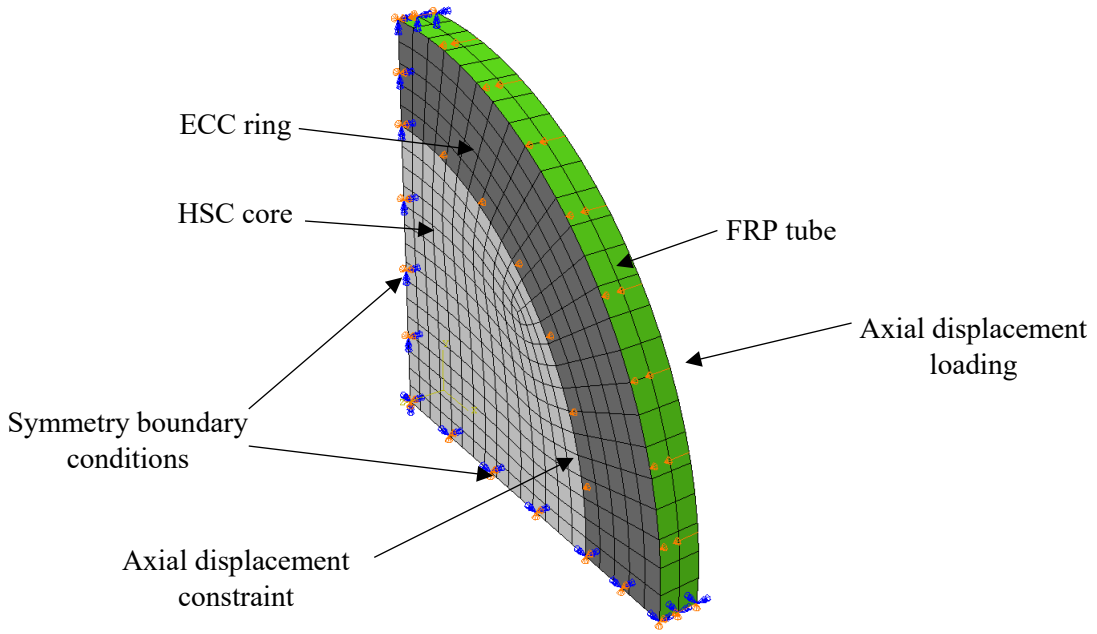

Fig. 9 Finite element model of FRP-ECC-HSC specimen

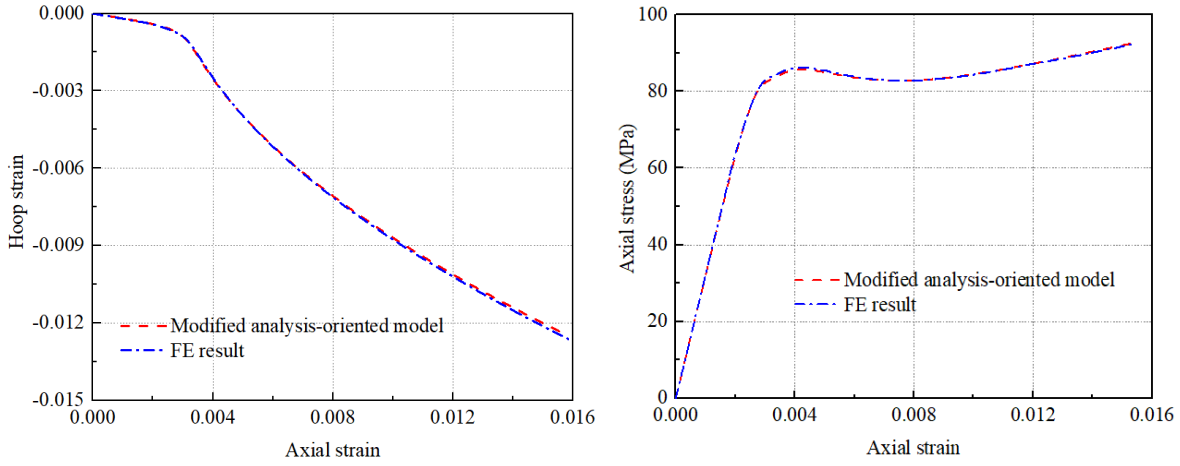

(a) FRP-confined HSC (C70)

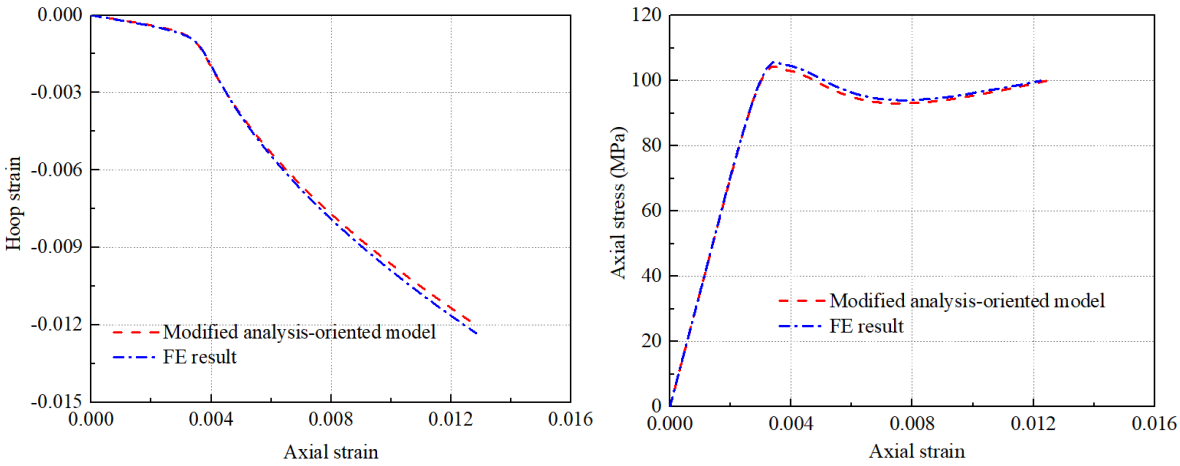

(b) FRP-confined HSC (C90)

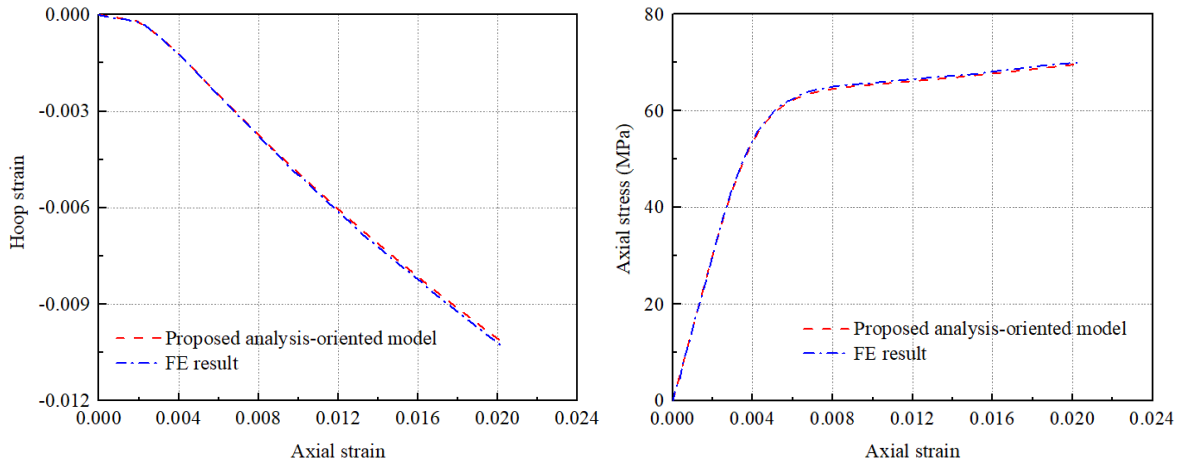

(c) FRP-confined ECC (E50)

Fig. 10 Comparisons between analysis-oriented model and FE result for uniformly FRP-confined concrete

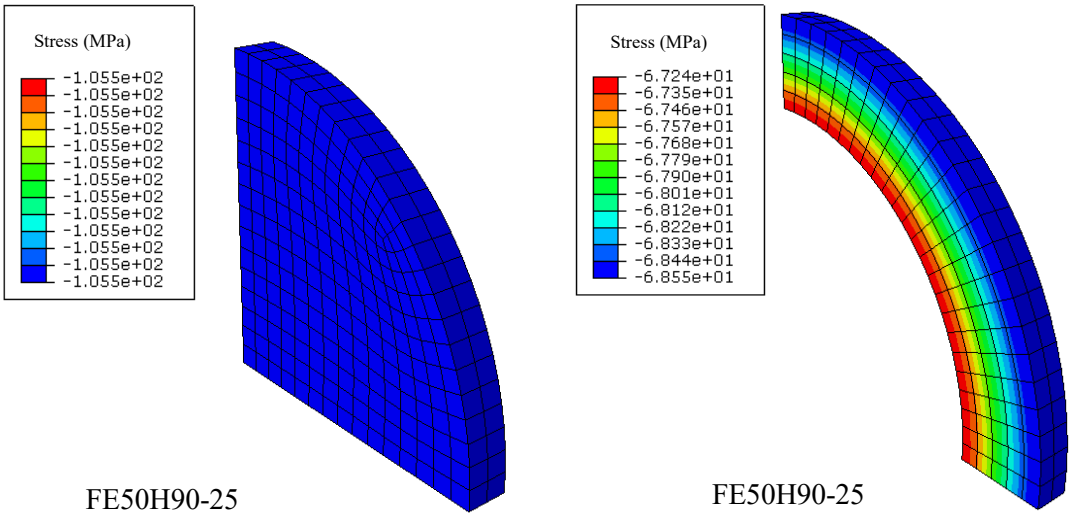

HSC core ECC ring

Fig. 11 Axial stress distribution over the section of FRP-ECC-HSC composite column

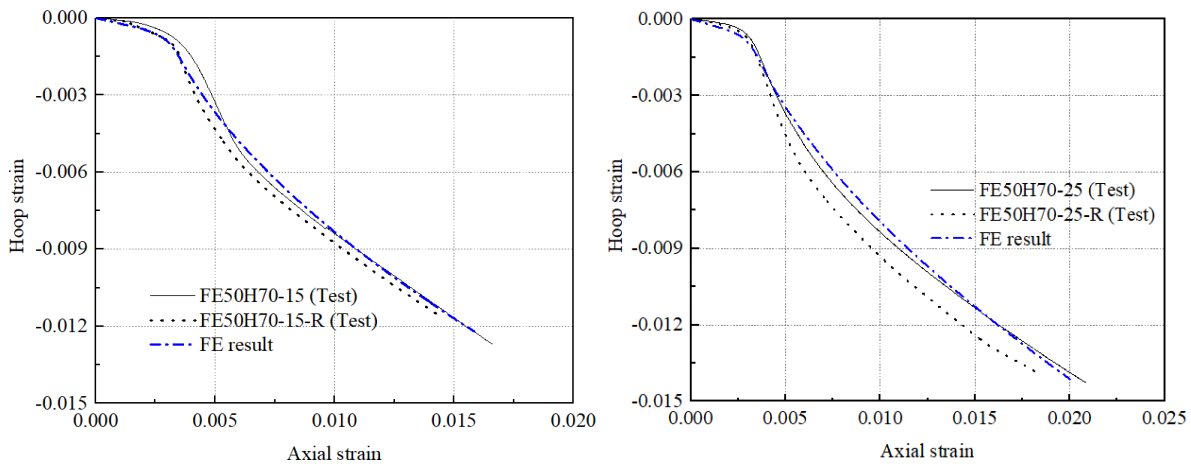

(a) FE50H70-15 (b) FE50H70-25

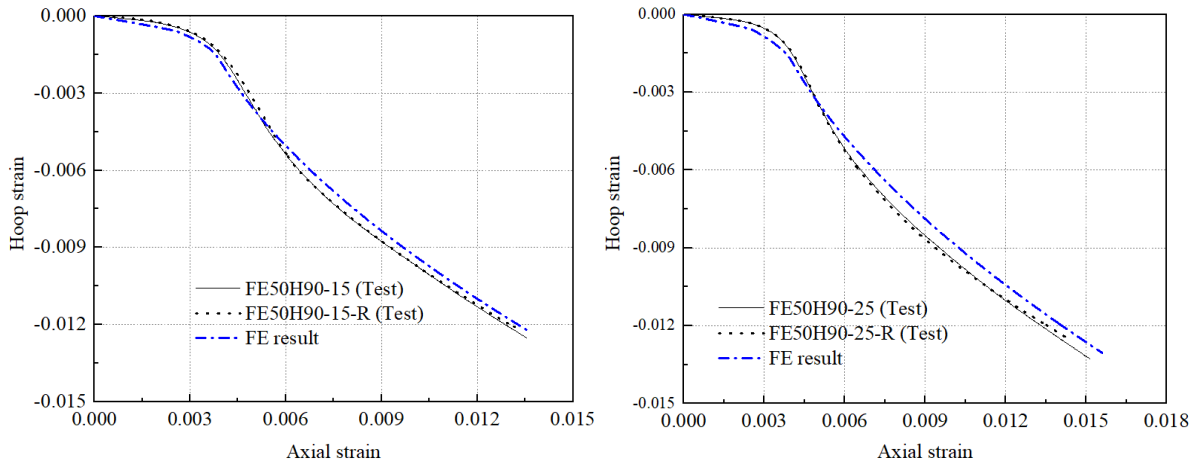

(c) FE50H90-15 (d) FE50H90-25

Fig. 12 Hoop strain-axial strain curves of FRP-ECC-HSC specimens

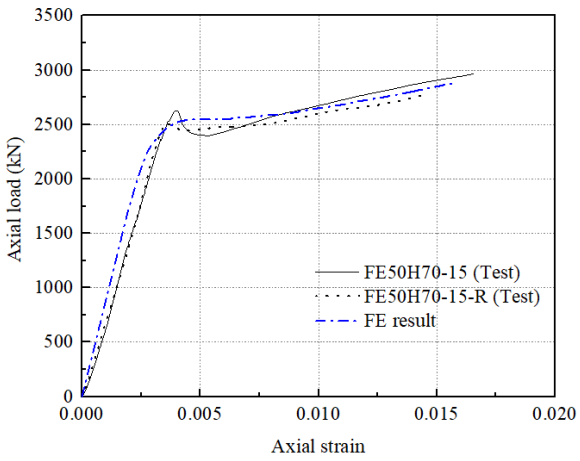

(a) FE50H70-15

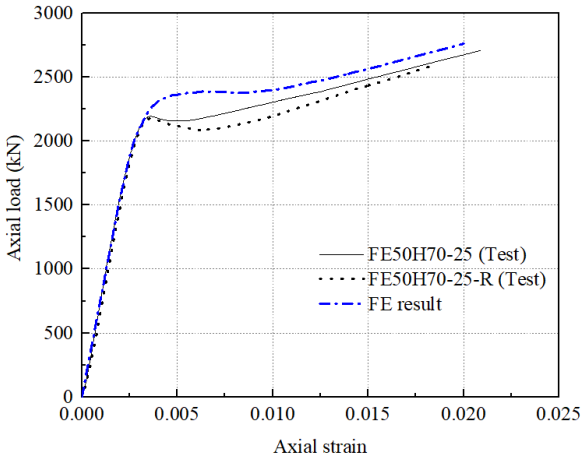

(b) FE50H70-25

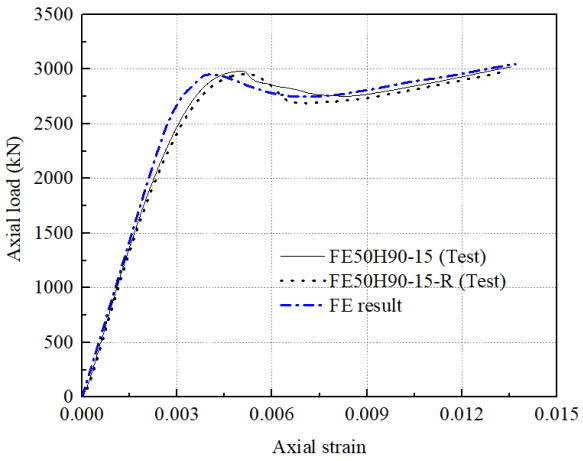

(c) FE50H90-15

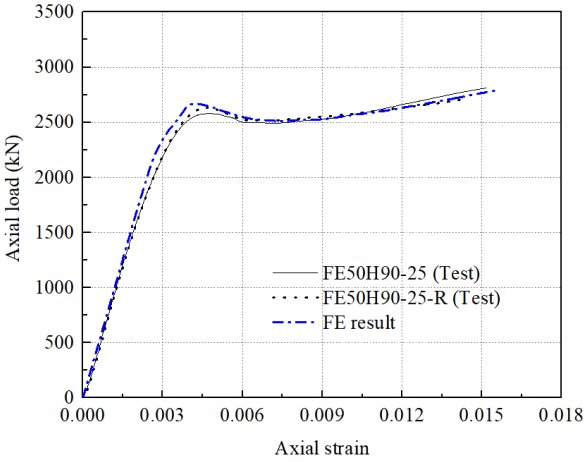

(d) FE50H90-25

Fig. 13 Axial load-axial strain curves of FRP-ECC-HSC specimens

Table 6 Ultimate conditions obtained by FE simulation and tests

Specimen ID	Ultimate load capacity (kN)			Ultimate axial strain		
	$F_{c,test}$	$F_{c,FE}$	$F_{c,FE}/F_{c,test}$	$\varepsilon_{cc,test}$	$\varepsilon_{cc,FE}$	$\varepsilon_{cc,FE}/\varepsilon_{cc,test}$
FH70	2791.9	3007.8	1.08	0.0144	0.0146	1.01
FH70-R	2862.3	3007.8	1.05	0.0152	0.0146	0.96
FE50H70-15	2966.0	2887.3	0.97	0.0166	0.0158	0.95
FE50H70-15-R	2773.3	2887.3	1.04	0.0145	0.0158	1.09
FE50H70-25	2706.5	2760.3	1.02	0.0209	0.0200	0.96
FE50H70-25-R	2582.5	2760.3	1.07	0.0185	0.0200	1.08

FH90	3165.5	3217.9	1.02	0.0123	0.0120	0.98
FH90-R	3172.3	3217.9	1.01	0.0124	0.0120	0.97
FE50H90-15	3021.3	3047.9	1.01	0.0137	0.0137	1.00
FE50H90-15-R	2972.0	3047.9	1.03	0.0133	0.0137	1.03
FE50H90-25	2809.2	2791.9	0.99	0.0152	0.0156	1.03
FE50H90-25-R	2709.5	2791.9	1.03	0.0144	0.0156	1.08
Mean			1.03			1.01
Cov			0.028			0.049

5. Discussions

5.1 Stress distribution on ECC ring

As illustrated in sections 2 and 4 of this paper, ECC ring is under non-uniform confinement, indicating the confining pressure varies at different locations in the ring region. Meanwhile, the stresses in the radial and circumferential directions are different. The distributions of radial stress and circumferential stress at the ultimate point are presented in Fig. 14. It can be observed that the radial stress will decrease with the increase of the distance from section center. For specimens with the same HSC core strength, radial stress will increase with the increase of ECC ratio. As for circumferential stress, on the contrary, it will increase with the increase of distance from the section center. Same as radial stress, circumferential stress is larger for the specimens with C70 as HSC core and 25 mm ECC thickness.

Based on the two principal stresses in the lateral direction, equivalent confining pressure is calculated with Eq. (49). Distribution of the calculated equivalent confining pressure is shown in Fig. 15. It can be observed that the equivalent confining pressure nearly remains unchanged at different locations in the ECC ring. It demonstrates that the adopted Eq. (49) can lead to a nearly uniform equivalent confining pressure distribution over the ring section, which is used to calculate the axial stress further.

Axial stress distribution is shown in Fig. 16 for the ECC ring of FRP-ECC-HSC specimens. Since the confining pressures are not identical at different locations in the ECC ring, the axial stresses will be not identical as well under the same axial strain. Therefore, the axial stress is non-uniformly distributed in the ECC ring. With the increase of distance from the section center, axial stress will increase accordingly. This is due to the fact that the equivalent lateral strain calculated based on Eq. (50) is lower for the outer locations, leading to the larger equivalent confining stiffness under the nearly same equivalent confining pressure. For the specimens with same ECC thickness, the one with C70 as the HSC core has larger axial stress than the one with C90 as HSC core. Meanwhile, for the specimens with the same HSC strength, a larger ECC ratio will lead to a larger axial stress. Compared with unconfined ECC, it can be noted that axial compressive strength is enhanced for the ECC ring in the composite column for all the cases.

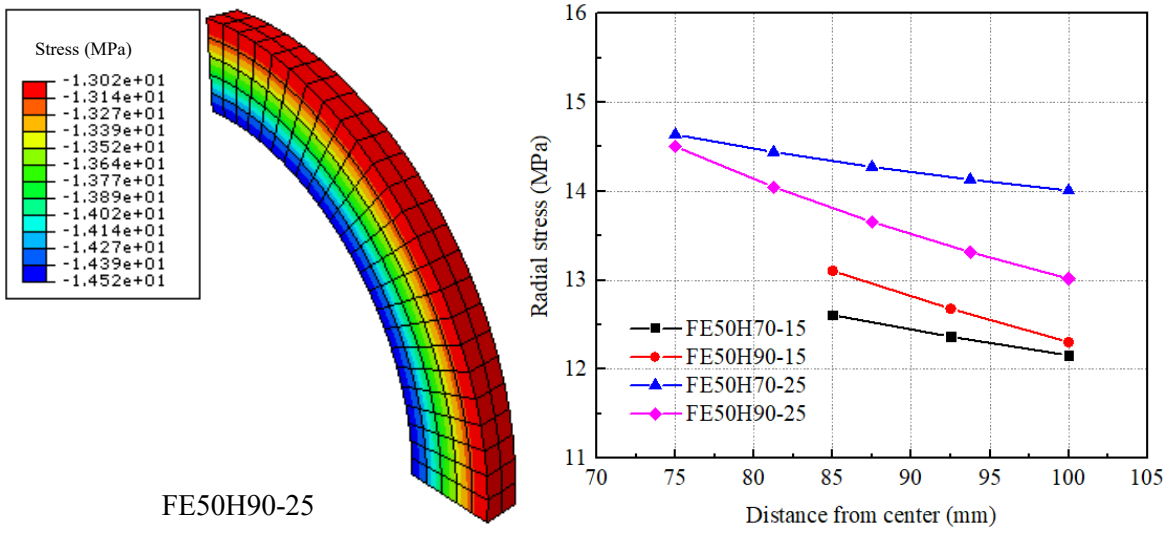

(a) Radial stress

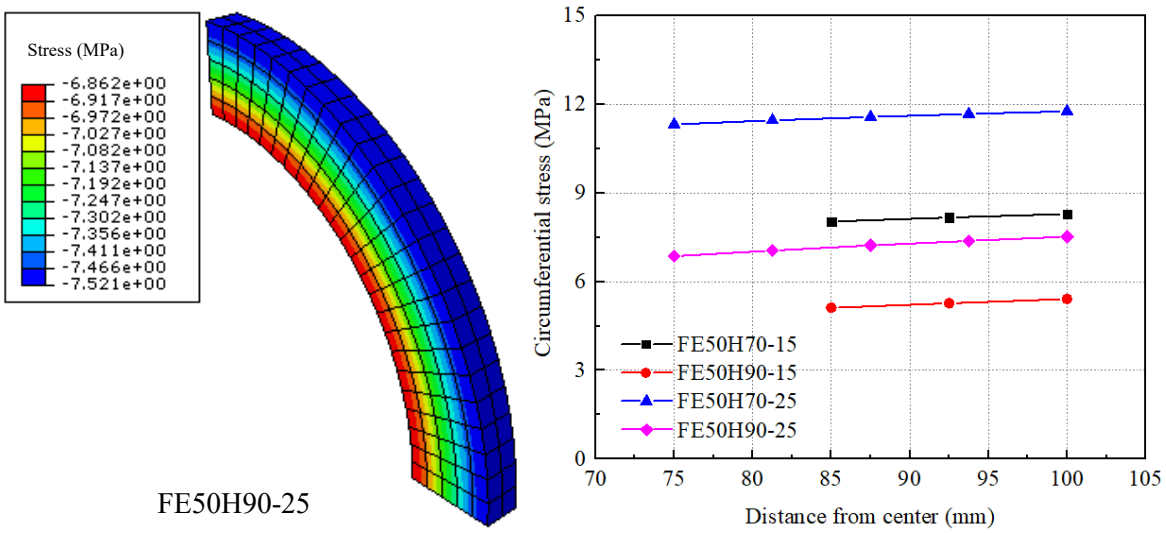

(b) Circumferential stress

Fig. 14 Lateral stress distributions of ECC ring

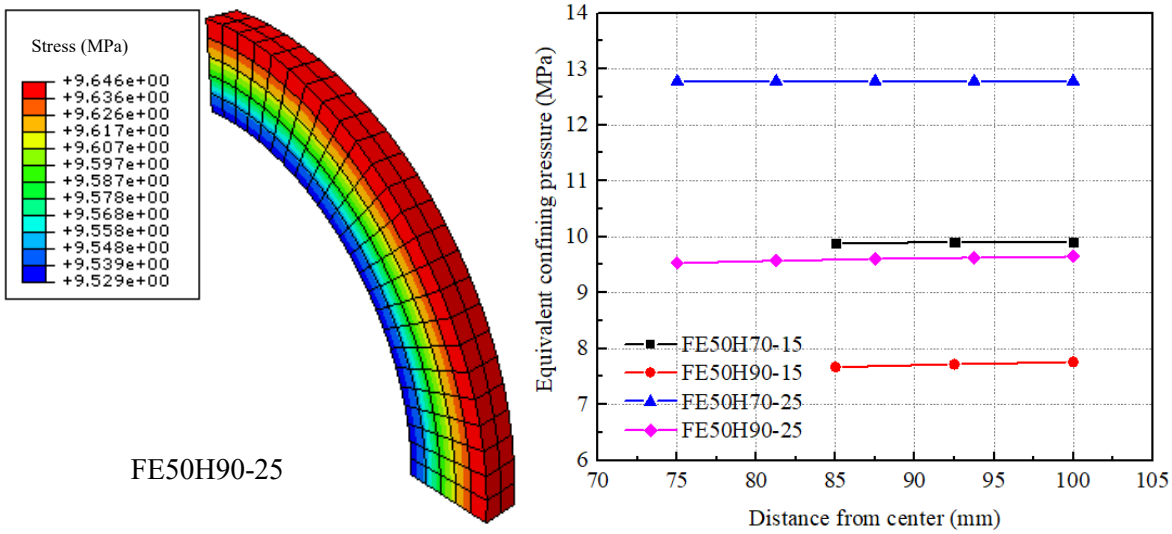

Fig. 15 Equivalent confining pressure distribution of ECC ring

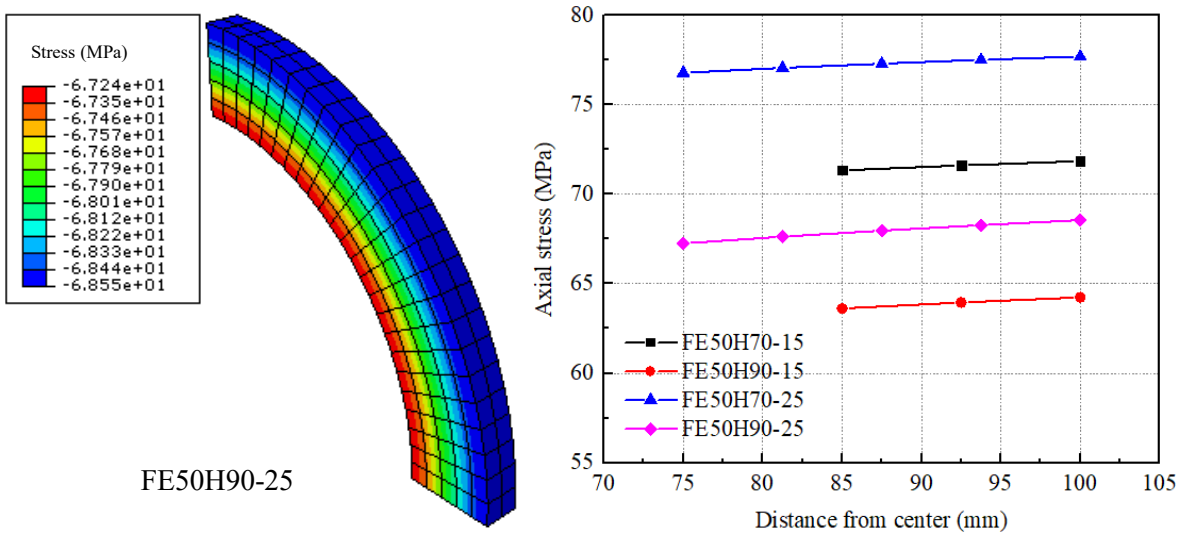

Fig. 16 Axial stress distribution of ECC ring

5.2 Confining pressure applied on HSC core

For normal FRP-confined concrete column, the confining pressure provided by FRP and applied on the concrete can be simply calculated by Eq. (19), using the actual FRP hoop rupture strain. According to the discussion of transfer coefficient k in section 2.2, the confining pressure applied on the HSC core for FRP-ECC-HSC composite column is larger than that provided by the FRP tube. Similar observation can be noted through FE simulations as well. Taking FE50H90-25 as an example, Fig. 17(a) shows the confining pressure applied on the HSC core and Fig. 17(b) shows the hoop tensile strain of the FRP tube that can be used to calculate the confining pressure provided by FRP tube with Eq. (19). Comparisons between the confining pressure applied on the HSC core and the confining pressure provided by the FRP tube are presented in Fig. 18 for different specimens. It is found that the confining pressure applied on HSC core is 5-13.7% larger than the confining pressure provided by the FRP tube, based on the FE results. It numerically indicates that a larger confining pressure applied on the inner HSC core can be produced for FRP-ECC-HSC composite column compared with normal FRP-confined HSC column, with the same column diameter and FRP tube thickness. Though

the mechanical analysis is conducted under the assumption of using elastic material properties while the FE analysis is using the actual elastic-plastic material properties, they both show the enhancement effect of the confining pressure applied on the inner core concrete as presented in Table 3 and Fig. 18. The enhancement ratio is larger for specimens with C90 as HSC core due to the larger difference of elastic modulus between HSC core and ECC ring. Meanwhile, it will also increase with the increase of ECC ratio.

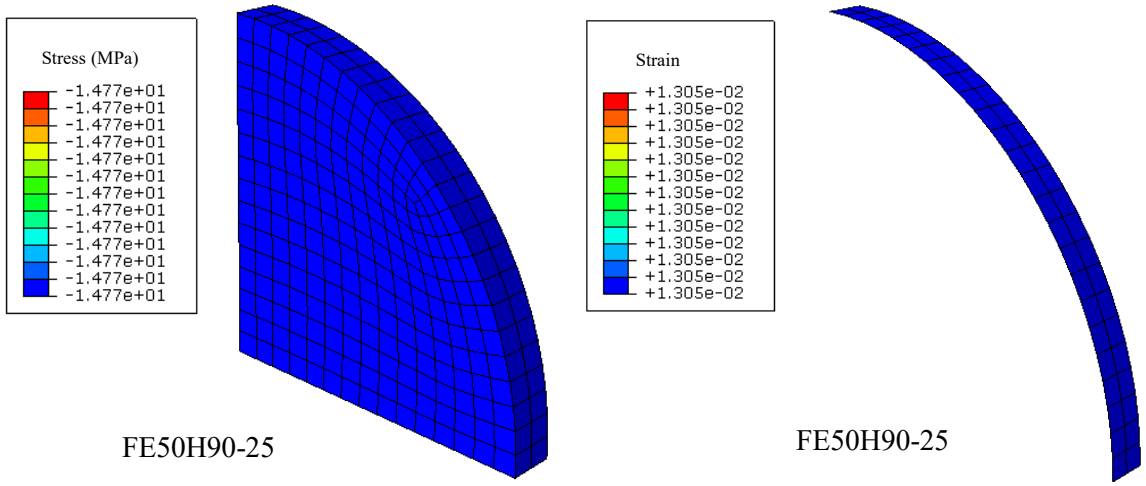

(a) Confining pressure on HSC core (b) Hoop tenisle strain on FRP tube

Fig. 17 Stress and strain on HSC core and FRP tube

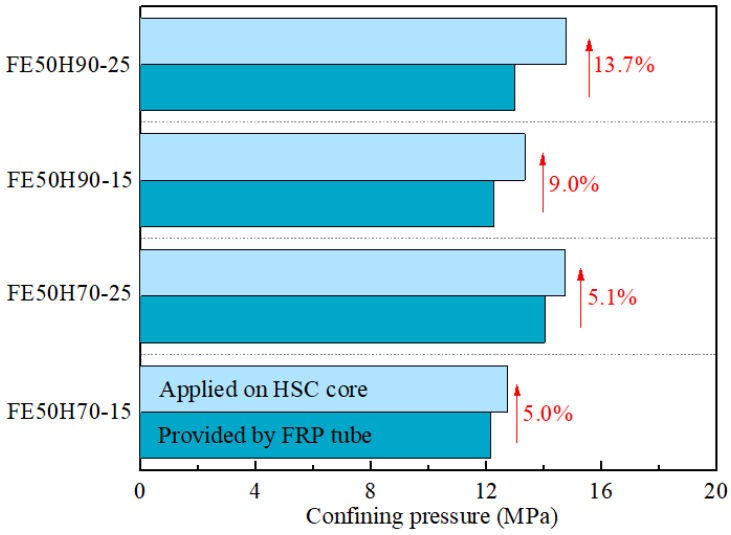

Fig. 18 Confining pressure obtained by FE simulations

5.3 Influence of ECC ratio

With the validated FE model, the influence of ECC ratio on the behavior of FRP-ECC-HSC composite column can be further investigated through parametric studies. Since the column failure is governed by FRP rupture in the hoop direction, rupture strain for different specimens, which is increased with the increase of ECC ratio as observed in tests, needs to be firstly determined. Linear relationship between rupture strain $\varepsilon_{h,rup}$ and ECC ratio α is assumed and regressed as shown in Fig. 19. It is worth noting that the rupture strain will also decrease with the increase of concrete strength. Therefore, different intercepts are assigned with the specimens with different HSC core strengths for the linear regression, while the same slope is adopted considering the same effect of ECC ratio. The linear relations are expressed as follows:

$$\varepsilon_{h,rup} = 0.00363\alpha + 0.0120 \qquad \text{for C70 as HSC core} \tag{52}$$

$$\varepsilon_{h,rup} = 0.00363\alpha + 0.0115 \qquad \text{for C90 as HSC core} \tag{53}$$

Different ECC ring thicknesses, ranging from 0-50 mm are assigned with the FRP-ECC-HSC specimens in FE models, yielding the ECC ratio from 0 to 0.75. C70 is adopted here as the HSC core, while ECC and FRP tube properties remain the same as the tested specimens as shown in Table 1. The ultimate points corresponding to the column failure are determined by the rupture strains presented in Fig. 19. Hoop strain-axial strain curves and axial load-axial strain curves are plotted in Figs. 20 and 21, respectively. It can be observed that with the increase of ECC ratio, the hoop strain will increase more slowly. Together with an improved rupture strain, it leads to a larger ultimate axial strain. When the ECC ratio increases from 0 to 0.75, the hoop rupture strain is increased by 23%, while the ultimate axial strain can be increased by 67%. The specimens with larger ECC ratio will have a lower initial stiffness and first peak load because of the lower strength and elastic modulus of ECC ring than those of HSC core. However, ultimate load capacity at FRP rupture decreases only within a limited

range with the increase of ECC ratio, since the improved axial strain extends the strain hardening stage. Therefore, it can be understood that the FRP-ECC-HSC composite column could achieve the similar capacity but much more enhanced deformability with the appropriate design of ECC ratio, compared with the corresponding FRP-confined HSC column. The FRP-ECC-HSC composite columns may exhibit the advantages over normal FRP-confined HSC columns under the extreme conditions, such as seismic loadings where the structural members are required to withstand relatively large deformations. Meanwhile, the novel composite column is steel-free and could be used in the marine environments without concerning corrosion problems. Seawater sea sand concrete can also be explored to be used in this composite column.

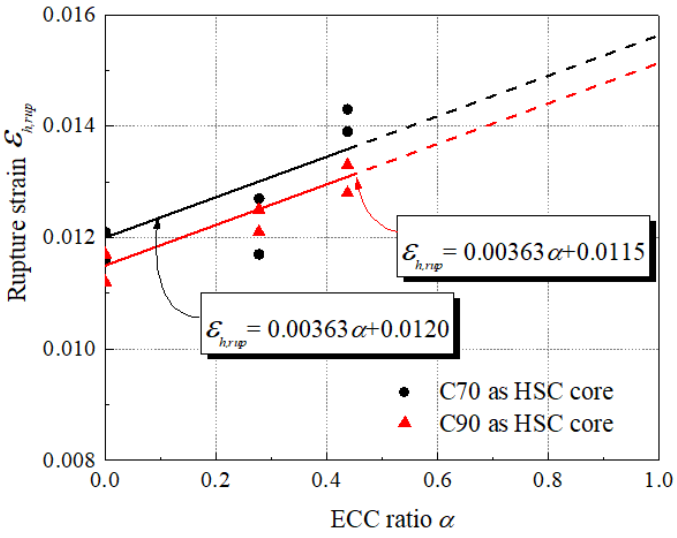

Fig. 19 Relationship between rupture strain and ECC ratio

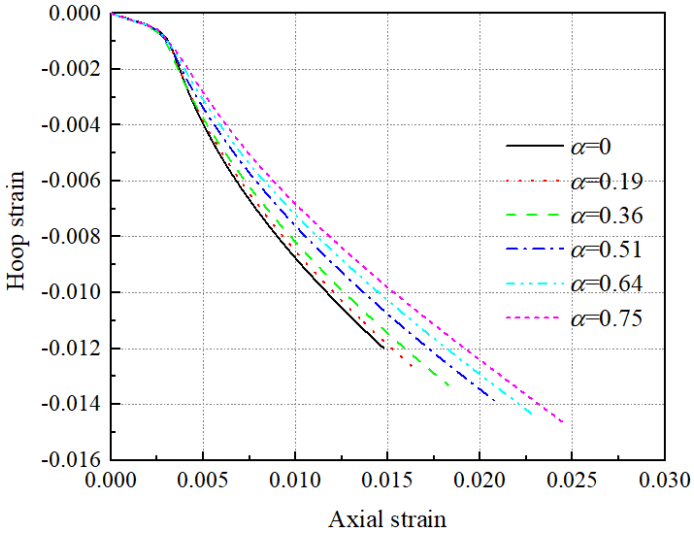

665

666 Fig. 20 Influence of ECC ratio on hoop strain-axial strain behavior

667

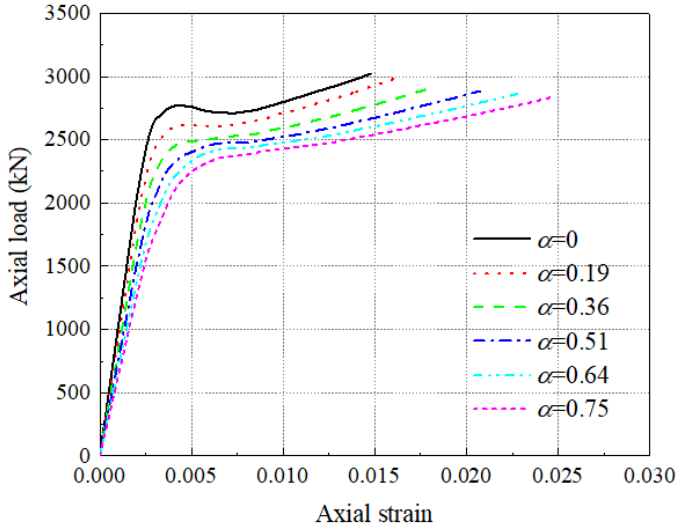

668

669 Fig. 21 Influence of ECC ratio on axial load-axial strain behavior

670

671 **6. Conclusions**

672 This study presents the mechanical analysis on the FRP-ECC-HSC composite column to obtain
673 the stress distribution and the confining pressure applied on HSC core and ECC ring. FE
674 models are developed using CDP model with accurate confined concrete properties to simulate

675 the behavior of FRP-ECC-HSC composite stub column under axial compression. The
676 following conclusions can be drawn:

677 (1) The radial stress and circumferential stress in the ECC ring are not equal, and they both
678 vary at different locations. Confining pressure applied on the HSC core is larger than
679 that provided by the FRP tube, and it increases with the increase of ECC ratio.
680 (2) The modified hoop strain-axial strain equation can provide closer predictions on the
681 dilation behavior of FRP-confined HSC in this study. Analysis-oriented model for FRP-
682 confined ECC is also proposed and compared with the available test data. Accurate
683 material properties were generated with the developed analysis-oriented models for
684 HSC and ECC in FE models.
685 (3) The predictions by FE models are in close agreement with the test results for the FRP-
686 ECC-HSC composite stub column. Stress distribution in the ECC ring, which is under
687 non-uniform confinement, can be clearly observed. Similar as the mechanical analysis,
688 it also demonstrates by the FE results that the confining pressure applied on the HSC
689 core is larger than the confining pressure provided by FRP tube.
690 (4) With the increase of ECC ratio, the FRP-ECC-HSC composite column could achieve a
691 much more improved ultimate axial strain, with the similar ultimate load carrying
692 capacity compared with the corresponding FRP-confined HSC column.

693

694 **CRediT authorship contribution statement**

695 **Shuai Li:** Investigation, Data curation, Writing - original draft. **Tak-Ming Chan:** Writing -
696 review & editing, Funding acquisition, Supervision. **Ben Young:** Writing - review & editing,
697 Funding acquisition, Supervision.

698

Declaration of Competing Interest

The authors declare that they have no known competing financial interests or personal relationships that could have appeared to influence the work reported in this paper.

Acknowledgement

The research work presented in this paper was supported by the Research Grants Council of the Hong Kong Special Administrative Region, China – Theme-based Research Scheme (Project No. T22-502/18-R).

References

[1] Zeng JJ, Ye YY, Gao WY, Smith ST, Guo YC. Stress-strain behavior of polyethylene terephthalate fiber-reinforced polymer-confined normal-, high- and ultra high-strength concrete. J Build Eng 2020;30:101243.

[2] Yang JQ, Feng P. Analysis-oriented model for FRP confined high-strength concrete: 3D interpretation of path dependency. Compos Struct 2021;278:114695.

[3] Ozbakkaloglu T, Lim JC, Vincent T. FRP-confined concrete in circular sections: Review and assessment of stress–strain models. Eng Struct 2013;49:1068–88.

[4] Ozbakkaloglu T, Akin E. Behavior of FRP-confined normal- and high-strength concrete under cyclic axial compression. J Compos Constr 2012;16(4):451-463.

[5] Li S, Chan TM, Young B. Experimental investigation on axial compressive behavior of novel FRP-ECC-HSC composite short column. Compos Struct 2023; 303:116285.

720 [6] Jiang T, Teng JG. Analysis-oriented stress-strain models for FRP-confined concrete. Eng.
721 Struct 2007;29:2968-2986.

722 [7] Lim JC, Ozbakkaloglu T. Unified stress-strain model for FRP and actively confined normal-
723 strength and high-strength concrete. J Compos Constr 2015;19(4):04014072.

724 [8] Ho JCM, Ou XL, Chen MT, Wang Q, Lai MH. A path dependent constitutive model for
725 CFFT column. Eng Struct 2020;210:110367.

726 [9] Cao YG, Zhang Y, Liu MY, Lu ZF, Jiang C. Analysis-oriented stress-strain model for FRP-
727 confined predamaged concrete. J Build Eng 2021;36:102121.

728 [10] Zhu JJ, Chen J, Chan TM. Analytical model for circular high strength concrete filled steel
729 tubes under compression. Eng Struct 2021;244:112720.

730 [11] Zakir M, Sofi FA, Naqash JA. Compressive testing and finite element analysis-based
731 confined concrete model for stiffened square FRP-concrete-steel double-skin tubular columns.
732 J Build Eng 2021;44:103267.

733 [12] Zhu JY, Lin G, Teng JG, Chan TM, Zeng JJ, LI LJ. FRP-Confined Square Concrete
734 Columns with Section Curvilinearization under Axial Compression. J Compos Constr
735 2020;24(2): 04020004.

736 [13] Lam L, Teng JG. Design-oriented stress-strain model for FRP-confined concrete. Constr
737 Build Mater 2003;17(6):471–89.

738 [14] Wei Y, Miao KT, Zhang X, Zhou YF, Zheng KQ. Modeling for complete stress-strain
739 curve of circular concrete columns confined with steel spiral and FRP. J Build Eng
740 2021;44:103294.

741 [15] Yu T, Teng JG, Wong YL, Dong SL. Finite element modeling of confined concrete-I:
742 Drucker–Prager type plasticity model. Eng. Struct 2010;32:665-79.

743 [16] Yu T, Teng JG, Wong YL, Dong SL. Finite element modeling of confined concrete-II:
744 Plastic-damage model. Eng. Struct 2010;32:680-91.

745 [17] Lo SH, Kwan AKH, Ouyang Y, Ho JCM. Finite element analysis of axially loaded FRP-
746 confined rectangular concrete columns. Eng. Struct 2015;100:253-263.

747 [18] Ribeiro F, Sena-Cruz J, Branco FG, Júlio E. 3D finite element model for hybrid FRP-
748 confined concrete in compression using modified CDPM. Eng. Struct 2019;190:459-479.

749 [19] Zeng JJ, Chen SP, Zhuge Y, Gao WY, Duan ZJ, Guo YC. Three-dimensional finite
750 element modeling and theoretical analysis of concrete confined with FRP rings. Eng. Struct
751 2021;234:111966.

752 [20] Hany NF, Hantouche EG, Harajli MH. Finite element modeling of FRP-confined concrete
753 using modified concrete damaged plasticity. Eng Struct 2016;125:1-14.

754 [21] Li BB, Jiang JF, Xiong HB, Zhan Y, Wu ZJ, Cunninghan LS. Improved concrete plastic-
755 damage model for FRP-confined concrete based on true tri-axial experiment. Compos Struct
756 2021;269:114051.

757 [22] Li Y, Wang W, Wen C. Experiment study on mechanical performance of ECC under
758 conventional triaxial compression. Concrete 2016;1:59–63.

759 [23] Dang Z, Feng P, Yang JQ, Zhang Q. Axial compressive behavior of engineered
760 cementitious composite confined by fiber-reinforced polymer. Compos Struct
761 2020;243:112191.

762 [24] Yuan WY, Han Q, Bai YL, Du XL, Yan ZW. Compressive behavior and modelling of
763 engineered cementitious composite (ECC) confined with LRS FRP and conventional FRP.
764 Compos Struct 2021;272:114200.

765 [25] Li S, Chan TM, Young B. Behavior of GFRP-concrete double tube composite columns.
766 Thin-Walled Struct, 2022;178:109460.

767 [26] Boresi AP, Schmidt RJ, Sidebottom OM. Advanced mechanics of materials (5th ed.).
768 1993;New York: Wiley.

769 [27] Teng JG, Huang Y, Lam L, Ye L. Theoretical model for fiber-reinforced polymer confined
770 concrete. J Compos Constr 2007;11(2):201–10.

771 [28] Popovics, S. A numerical approach to the complete stress-strain curve of concrete. Cement
772 and Concrete Research, 1973;3:583-599.

773 [29] Lim JC, Ozbakkaloglu T. Stress-strain model for normal and light-weight concretes under
774 uniaxial and triaxial compression. Constr Build Mater 2014;71:492–509.

775 [30] Lim JC, Ozbakkaloglu T. Later strain-to-axial strain relationship of confined concrete. J
776 Struct Eng 2014; 04014141.

777 [31] Lai MH, Ho JCM. A theoretical axial stress-strain model for circular concrete-filled-steel-
778 tube columns. Eng. Struct 2016;125:124-243.

779 [32] Zhang B, Yu T, Teng JG. Behavior of concrete-filled FRP tubes under cyclic axial
780 compression. J Compos Constr 2015;19(3):04014060.

781 [33] Zhang B, Hu ZM, Zhao Q, Huang T, Zhang NY, Zhang QB. Effect of fiber angles on
782 normal and high-strength concrete-filled fiber-reinforced polymer tubes under monotonic axial
783 compression. Adv Struct Eng 2020;23(5):924-940.

784 [34] ABAQUS. ABAQUS Analysis User's Manual, version 2017; 2016.

785 [35] Contrafatto L, Cuomo M. A framework of elastic–plastic damaging model for concrete
786 under multiaxial stress states. Int J Plast 2006;22:2272–300.

787 [36] Lubliner J, Oliver J, Oller S, Onate E. A plastic-damage model for concrete. Int J Solid
788 Struct 1989;25:299–329.

789 [37] Lee J, Fenves GL. Plastic-damage model for cyclic loading of concrete structures. J Eng
790 Mech, ASCE 1998;124(8):892–900.

791 [38] Ozbakkaloglu T, Gholampour A, Lim JC. Damage-Plasticity Model for FRP-confined
792 normal-strength and high-strength concrete. J Compos Constr 2016;20(6):04016053.

793 [39] Jiang JF, Wu YF. Identification of material parameters for Drucker–Prager plasticity
794 model for FRP confined circular concrete columns. Int J Solid Struct 2012;49:445-456.

795 [40] Kupfer H, Hilsdorf HK, Rusch H. Behavior of concrete under biaxial stresses. ACI J
796 1969;66:656–66.